POLITECNICO DI TORINO

Master's Degree in Biomedical Engineering

Master's Degree Thesis

Design and Development of Inductive Wireless Power Receivers for Implantable Neural Interfaces

Supervisors

Prof. Danilo Demarchi

Prof. Paolo Motto Ros

M.Sc. Andrea Dentis

Candidate

Giada Navarra

JULY 2026

Abstract

Implantable medical devices have become an essential technology for the treatment and monitoring of a wide range of medical conditions, including cardiac disorders, neurological diseases, and sensory impairments. Traditionally, these devices rely on implanted batteries, whose limited lifetimes often require periodic surgical replacements. Such procedures increase healthcare costs and expose patients to additional risks, including infection and surgical complications. Wireless Power Transfer (WPT) offers a promising alternative by enabling transcutaneous energy delivery, extending battery lifetime or, in some applications,eliminating the need for an implanted battery.

This thesis presents the design and development of two receivers intended to be used in an Inductive WPT system. The two receivers were designed around the power requirements of the Intan Technologies RHS2116. The proposed architectures provide the supply rails required by the target applications: ± 3.3 V in one configuration and $+3.3$ V together with ± 7 V in the other.

The primary objective was to maximize the overall circuit efficiency at low power transmission levels. The design process started with LTSpice simulations, integrated with MATLAB and Python environments to optimize design choices. Each receiver consists of four main blocks: a receiving coil with a resonant capacitor tuned at 13.56 MHz, an impedance matching network, a class-E rectifier, and a DC/DC conversion stage. The efficiency of each block was evaluated by comparing its input and output power, while the overall efficiency of the system was calculated as the ratio between the total power delivered to the regulated loads and the power supplied by the transmitter source.

Afterwards, the Printed Circuit Boards (PCBs) were designed using Altium Designer. During the layout process, key constraints such as compact form factor, thermal management, and high-frequency signal integrity were considered. Once the PCBs were fabricated, experimental tests were performed under different load conditions.

Measurements were performed with the transmitter and receiver coils aligned at a separation distance of 10 mm. For the ± 3.3 V receiver, designed to operate over an output power range from 16 mW to 100 mW, the overall efficiency increased, respectively, from 10.5% to 33.9%. For the ± 7 V receiver, the overall efficiency increased from 8.9% at the minimum design output power of 24 mW to 19.4% at the maximum design output power of 100 mW. Consistently with the SPICE simulation results, the efficiency was observed to increase as the load power increased. The experimental results also demonstrate that proper matching network tuning can significantly enhance the overall system efficiency.

Acknowledgements

First of all, I would like to thank my supervisors Paolo Motto Ros, Andrea Dentis and Danilo Demarchi for giving me the chance to work on such an interesting project and teaching me more than I could have imagined. I would also like to thank the students and PhD students at DET for showing me how much kindness can help people, even during the most challenging moments.
Lastly, a huge thanks to my family, my friends and my boyfriend, for being there for me, no matter the distance. You have never left my hand throughout this journey. This thesis carries a piece of each of you.

Contents

Acronyms

AIMD	Active Implantable Medical Device
CWPT	Capacitive Wireless Power Transfer
DUT	Device Under Test
EMI	Electromagnetic interference
ENG	Electroneurographic
HFSS	High frequency structure simulator
IMD	Implantable Medical Device
IWPT	Inductive Wireless Power Transfer
NCC	Near-Field Capacitive Coupling
NRIC	Near-Field Resonant Inductive Coupling
PCB	Printed Circuit Board
PP	Parallel-Parallel
PS	Parallel-Series
PTE	Power Transfer Efficiency
RCWPT	Resonant Coupled Wireless Power Transfer
RX	Receiver
SAR	Specific Adsorption Rate
SP	Series-Parallel
SS	Series-Series
TX	Transmitter

UTET Ultrasonic Transcutaneous Energy Transfer

VNA Vector Network Analyzer

WPT Wireless Power Transfer

WPT Zero Phase Angle

ZVS Zero Voltage Switching

List of Tables

List of Figures

Chapter 1

Introduction

Active implantable medical devices (AIMDs) are playing an increasingly vital role in treating and monitoring a variety of neurological [1], cardiovascular [2], and sensory disorders [3]. Recent advances in microelectronics have enabled the development of smaller and more sophisticated implants that can record physiological signals, provide therapeutic stimulation, and communicate wirelessly with external systems. However, the operational capacity of such devices remains significantly constrained by their power supply. [4]

Traditionally, implantable systems have relied on batteries, which have a limited lifespan and often require periodic surgical replacements. These procedures not only increase healthcare costs, but also expose patients to additional risks, such as infections, discomfort, and surgical complications. For this reason, Wireless Power Transfer (WPT) has emerged as a promising solution, enabling the delivery of transcutaneous energy without physical connections and potentially eliminating the need for implanted batteries.

Among the various WPT technologies, inductive coupling represents one of the most commonly used methods for biomedical implants due to its relatively high efficiency, safety, and compatibility with biological tissues [5]. Nevertheless, achieving high efficiency remains challenging, particularly in low-power applications where the available transmitted power is limited and the receiver dimensions must be kept as small as possible. In inductive wireless power transfer (IWPT), the power transfer efficiency is limited by the short operating distance between the coils and decreases in the presence of coil misalignment and biological tissues. Moreover, although a larger receiving coil generally increases the coupling coefficient, and therefore improves power transfer, the receiver size must be minimized to ensure better integration within the implantable system. [6]

This thesis focuses on the design, simulation, implementation, and experimental validation of two inductive wireless power receivers specifically intended for implantable neural interfaces operating at the 13.56 MHz ISM frequency. This work is part of the European NerveRepack project and the Rewire project, both aimed at developing advanced neuroprosthetic systems capable of restoring communication between the nervous system and external assistive devices.

The proposed receivers were designed around the power requirements of the Intan Technologies RHS2116 neural interface chip. [7] Two different architectures were developed: a first receiver providing dual supply rails of ± 3.3 V for the NerveRepack application and

a second receiver providing +3.3 V together with ±7 V rails for the Rewire application. The design process combines circuit simulations in LTSpice with MATLAB and Python-based analysis to optimize the receiving coil, matching network, Class-E rectifier, and DC/DC conversion stages. The optimized circuits were then implemented on Printed Circuit Boards (PCBs) using Altium Designer and experimentally characterized under different loading and misalignment conditions.
The aim of this thesis is to maximize the overall efficiency of the receiving system while following the constraints imposed by implantable biomedical applications.
Chapter 2 provides the theoretical background required to understand wireless power transfer systems for implantable biomedical devices. The NerveRepack and Rewire projects are introduced, followed by an overview of wireless power transfer techniques, inductive coupling principles, power transfer efficiency, and the main constraints associated with biomedical applications.
Chapter 3 presents the design methodology, starting from the load requirements derived from the Intan RHS2116 neural interface chip and continuing with the design of the receiving coil, impedance matching network, Class-E rectifier, and DC/DC conversion stages.
Chapter 4 presents the LTSpice simulations carried out to validate the proposed architectures and evaluate the efficiency of each functional block under different operating conditions.
Chapter 5 describes the implementation of the receivers on printed circuit boards using Altium Designer. Both electrical schematics and PCB layouts are discussed, highlighting the design choices adopted to improve signal integrity and minimize losses.
Chapter 6 reports the experimental validation of the fabricated prototypes. Measurements performed under different load conditions, as well as vertical, lateral, and angular coil misalignments, are presented and compared with the simulation results.
Finally, Chapter 7 summarizes the main achievements of this work and discusses possible future developments and improvements of the proposed wireless power receivers.

Chapter 2

Theoretical Background

2.1 Active implantable biomedical devices

The aging population, combined with the diversity of neurological and cardiovascular diseases that cannot be treated with traditional medication alone have increased the demand for long-term diagnostic and therapeutic solutions. Implantable Medical Devices (IMDs) have consequently become an important area of biomedical engineering, enabling continuous physiological monitoring, targeted stimulation, and controlled drug delivery. Neurological disorders alone affected more than three billion people worldwide in 2021, highlighting the need for innovative technologies capable of supporting long-term treatment and monitoring [8].

AIMDs represent a specific category of IMDs that rely on a source of energy other than that generated by the human body or gravity. These devices are intended to be fully or partially introduced into the human body and to remain in place after the implantation procedure [9]. Since AIMDs perform critical diagnostic or therapeutic functions, their design must satisfy stringent requirements concerning safety, reliability, biocompatibility, power consumption, and long-term operation. The development of implantable electronics began with cardiac applications. The first fully implantable cardiac pacemaker was implanted in Sweden in 1958, representing a major milestone in medical technology [10]. Since then, advances in microelectronics, materials, sensing, and low-power circuit design have considerably expanded the range of implantable applications. Current IMDs include cardiac pacemakers [11], cochlear implants [12], deep-brain and peripheral-nerve stimulators [13], glucose sensors [14], intracranial-pressure monitors [15], and capsule-endoscopy systems. [16] [17]

Recent technological progress has enabled implantable devices to become smaller, more intelligent, and more connected. Modern implants can acquire physiological signals, perform local data processing, deliver adaptive therapies, and communicate wirelessly with external equipment. Wireless communication and power transfer are therefore key technologies for the development of the next generation of AIMDs [18, 19]. In particular, wireless power can reduce the dependence on implanted batteries, which often represent one of the main limitations in terms of device size and operational lifetime, while potentially reducing the need for surgical battery replacement [17].

2.2 NerveRepack and Rewire projects

Implantable neural interfaces and neurostimulation devices represent one of the main technologies for restoring impaired functions of the nervous system. These systems can record neural activity, provide electrical stimulation, or combine both functions in closed-loop architectures, enabling bidirectional communication between the nervous system and external devices. Peripheral nerve interfaces are particularly relevant in the context of neuroprosthetics because they can be used to decode motor intentions and to provide sensory feedback, improving the interaction between the user and an artificial limb. [20, 21].
Despite their potential, implantable neurostimulation systems impose strict design constraints in terms of size, power consumption, reliability and biocompatibility. One of the main limitations is related to the power supply. Conventional implanted batteries increase the device volume and may require surgical replacement, exposing the patient to additional risks and discomfort. For this reason, wireless power transfer has become an attractive solution for implantable medical devices, because it can reduce, or even eliminate, the need for large implanted batteries while allowing transcutaneous energy delivery [22].
Within this framework, this thesis is related to two research projects: NerveRepack and Rewire. Both projects aim to develop advanced implantable interfaces for restoring neural communication and functionality, but they differ in terms of target application, power requirements and output voltage specifications.

The NerveRepack project is an European Union co-funded research initiative focused on the development of advanced implantable interfaces that enable bidirectional communication between the nervous system and mechatronics structures. The project addresses a major challenge faced by individuals with amputations or paralysis: the inability to effectively interface the damaged nerves with external assistive technologies such as prostheses and exoskeletons. It aims to restore both motor control and sensory feedback by re-establishing the connection between their nerves and advanced prosthetic limbs or exoskeletons.[23]

The Rewire project aims to restore functionality in damaged peripheral nerves affected by trauma or pathology conditions. The goal is to develop a device capable of recording electroneurographic (ENG) signals upstream of the lesion, processing and interpreting the information, and providing actuation by stimulating the nerves or muscles below the lesion or controlling a robotic prosthesis. To achieve this goal, the system must support wireless bidirectional data communication, configurable recording and stimulation settings, and be suitable for long-term implantation. The design of such a device requires careful optimization of size, power consumption, reliability like size, power consumption, and biocompatibility. In particular, balancing the power requirements of the neural recording interface, signal processing circuitry, and communication modules is essential to ensure efficient operation while maximizing battery lifetime or enabling the use of energy harvesting techniques. [24]

In this context, the developed receivers are intended to operate as the implanted power receiving units for these applications. Their role is to collect the energy transmitted wirelessly by the external transmitter unit, convert it into DC power, and provide the regulated supply voltages required by the implantable electronics, represented by the RHS2116.

2.3 Wireless Power Transfer Classifications

Wireless Power Transfer (WPT) represents a promising solution for powering AIMDs. It enables implanted batteries to be recharged without physical connections and may also support batteryless operation, in which the implant is powered directly by an external source through a wireless link [25]. Consequently, WPT can reduce the need for battery-replacement surgeries, limiting healthcare costs, patient discomfort, and the risk of infections or other complications [26]. Several WPT techniques have been developed and can be classified according to the physical mechanism used to transfer energy. WPT systems are typically divided into near-field and far-field links. The far-field electromagnetic radiation dominates at greater distances, while the non radiative near-field behaviors dominate when close to antennas or scattering objects. [27] For antennas much shorter than the wavelength, λ, the near-field and far-field regions can be approximated as in Fig 2.1. [28]

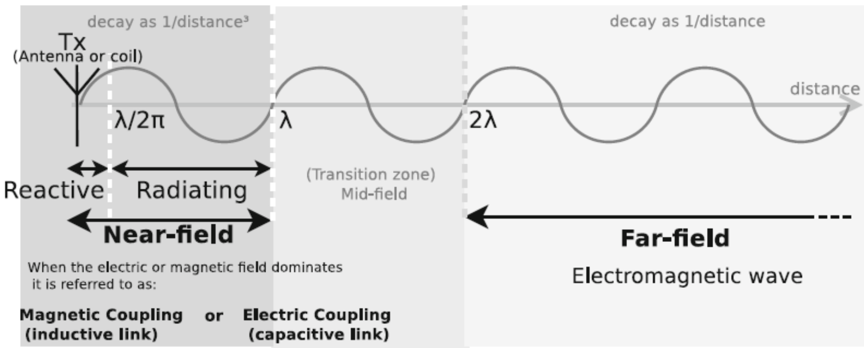

Figure 2.1. Near and far-field approximated regions for antennas much shorter than λ

The region between the near-field and the far-field is called the transition zone or mid-field, which has a combination of the characteristics of the near-field and the far-field. [29] Far-field is preferred when it is necessary to achieve long distances, in the range of meters, because the beam can be pointed toward the receiver. So, this is a beam-based WPT system that can transfer large power (kilowatts) at large distances (tens of meters) with high efficiency (>50%) at the risk of interference with other radio signals [30]. However, near-field links that do not require a line-of-sight operation are preferred for short distances (tens of centimeters), achieving higher efficiencies. [31]
Figures 2.2 and 2.3 show, respectively, WPT classifications and their applications.

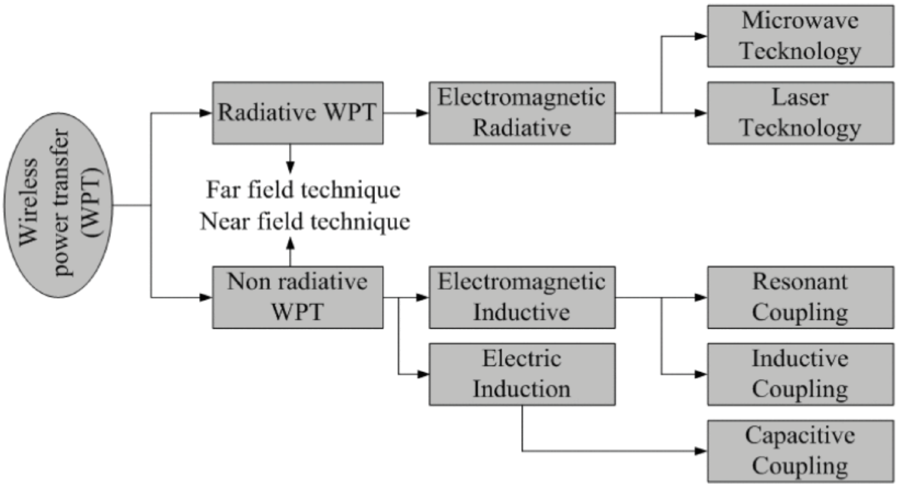

Figure 2.2. Different techniques of WPT [32]

Figure 2.3 shows WPT systems applications.

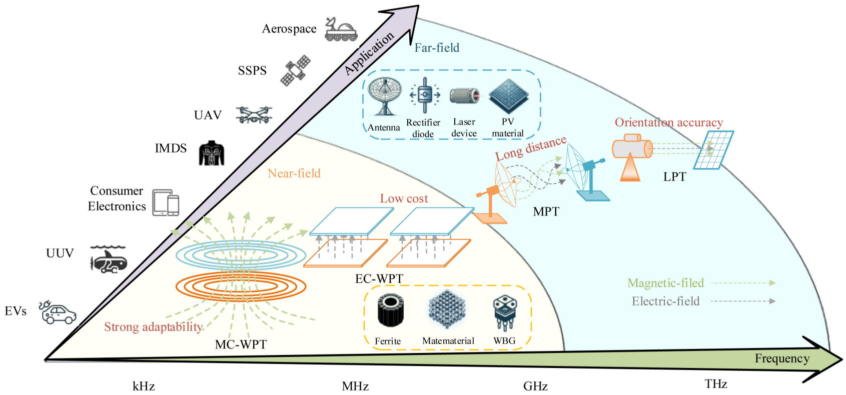

Figure 2.3. Overview diagram of a typical WPT system. [33]

The radiative power transfer method is not frequently used in civilian applications because its radiations might be harmful to human health. [32] For this reason, only the near-field techniques will be analyzed in 2.3.1.

2.3.1 Near-field WPT techniques

Capacitive wireless power transfer (CWPT), resonant coupled wireless power transfer (RCWPT), inductively coupled wireless power transfer (ICWPT), are three categories of non radiative WPT [32], so they are the most relatable for AIMDS.

Near-Field Capacitive Coupling (NCC) operates through electric-field coupling, where energy is transferred via the electric field established between conductive electrodes. The amount of power transfer is comparatively less than ICWPT and RCWPT. The capacitive coupling can be used for low power applications. However, due to its physical limitations related to the coupling capacitance and air-gap distance. It is generally suitable for very small gaps, typically below 1 mm. [34] During capacitive coupling, a small capacitance made by the electrodes gives a very high voltage between the electrodes, subjected to air breakdown. Furthermore, the external magnetic field does not affect the capacitive coupling. The use of the NCC method may result in additional power losses within the human body since it has been demonstrated that, above 100 kHz, electromagnetic energy absorption in biological tissues increases, potentially causing tissue heating. [35].

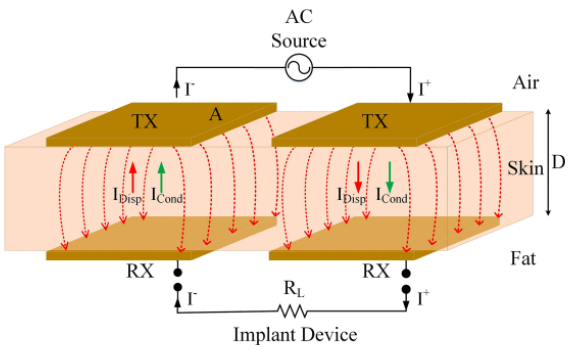

Figure 2.4. NCC method schematic. [36]

RCWPT technique generally operates at higher frequencies, typically in the MHz range, allowing power transfer over medium distances, even when the distance between the coils is comparable to or greater than their dimensions. RCWPT can provide higher efficiency over longer distances and better tolerance to coil misalignment. However, its performance strongly depends on the quality factor of the resonant coils and on accurate frequency tuning. Moreover, the use of MHz-range frequencies makes the implementation of high-power electronics more challenging due to switching losses, cost, and safety constraints. [37]

Near field resonant inductive coupling (NRIC) is a magnetic field powering method, using RF in the near-field region. It operates at frequencies from a few kHz to a few GHz. So far, IPT is the most commonly used WPT approach in implantable medical devices, since radio frequency in the near-field is less attenuated by the human tissues.

After comparing the main near-field WPT techniques, inductive wireless power transfer appears to be the most suitable solution for AIMDs [22, 38]. Compared to capacitive WPT, inductive coupling is less affected by the dielectric properties of biological tissues and does not require very small electrode gaps. In capacitive systems, the power transfer capability is strongly limited by the low coupling capacitance, while the use of electric

fields introduces additional safety concerns related to tissue absorption and heating [22, 31].
Compared to RCWPT, IWPT generally offers a simpler and more robust implementation, especially for short transmission distances. Although resonant coupling can improve the transfer distance and misalignment tolerance, it requires high quality resonators and accurate frequency tuning, making the system more sensitive to variations in coil positioning, load conditions, and tissue environment [22, 39]. The characteristics of NRIC will be described in 2.3.2.

2.3.2 NRIC Physical Principles and Structure

The physical principle behind inductive WPT is based on electromagnetic induction. An alternating current flowing through the primary coil (TX) generates a time-varying magnetic field. When a secondary coil (RX) is placed in close proximity to the transmitter, part of this magnetic field links with the receiver coil and induces an alternating voltage and current in it. In this way, electrical energy can be wiressly transferred from the primary coil to the secondary coil and used to power AIMDs. [26, p. 743]
This mechanism is described by Faraday's law of induction, which states that a time-varying magnetic flux induces an electromotive force across a conductor [28]

$$\varepsilon = -\frac{d}{dt}\int_{\Sigma} \vec{B} \cdot d\vec{A} \tag{2.1}$$

The physical quantities are defined as follows:

- ε: induced electromotive force (e.m.f.), measured in Volts [V];
- t: time, measured in seconds [s];
- $\vec{B}$: the magnetic induction vector (or magnetic flux density), measured in Tesla [T];
- $d\vec{A}$: infinitesimal area element of surface Σ, oriented according to the surface normal;
- $\int_{\Sigma} \vec{B} \cdot d\vec{A}$: the magnetic flux Φ_B linked with the surface Σ, measured in Weber [Wb].

A time-varying current flowing through a conductor generates a changing magnetic field, which induces a voltage across the conductor itself. This phenomenon, known as self-induction, becomes particularly significant when the conductor is in the form of a loop. A coil, which is a fundamental component of inductive WPT systems, consists of multiple loops connected in series. In circuit theory, this effect is characterized by the self-inductance L. For a sinusoidal current with amplitude I and frequency f, the amplitude of the sinusoidal voltage is given by $v_1 = 2\pi f LI$ [28] If a second conductor is exposed to the varying magnetic flux that is generated by the varying current in the first conductor, a varying voltage is induced across the second conductor as well. The current passing through the first conductor produces an induced voltage in the second conductor, modeled by a parameter, known as mutual inductance (M). Assuming a sinusoidal excitation current (i) at a certain frequency f passing through the first inductor, the induced voltage

across the second conductor would be $v_2 = iM2\pi f$. [28]
In IWPT systems, one of the most important parameters is the coupling coefficient, k, which describes the degree of magnetic coupling between the transmitter and receiver coils. It is defined as the mutual inductance M normalized with respect to the self-inductances of the two coils [28]:

$$k = \frac{M}{\sqrt{L_1 L_2}}. \tag{2.2}$$

where L_1 and L_2 are the self-inductance of each coil and M is the mutual inductance between them. The coupling coefficient k is a normalized parameter ranging from 0 to 1 that quantifies the strength of the magnetic coupling between two coils. Its value depends on their geometrical characteristics and relative position, including their dimensions, separation distance, alignment, and orientation. When $k = 0$, the coils are completely uncoupled, and the current flowing through one coil has no effect on the other. On the other hand, $k = 1$ represents ideal magnetic coupling, in which all the magnetic flux generated by one coil links the other coil. [28]
13.56 MHz was chosen as the carrier frequency, which is in the worldwide ISM band range to avoid tissue damage. [40] Also, coil antennas operating at 13.56 MHz, achieved remarkable miniaturization despite the low operating frequency. [41] [42]
The receiver must be tuned at the same resonant frequency as the transmitter:

$$f_{\text{res}} = \frac{1}{\pi\sqrt{L_1 C_1}} = \frac{1}{\pi\sqrt{L_2 C_2}} \tag{2.3}$$

A typical power transmission block diagram for inductive WPT systems used for AIMDs consists of two parts: the transmitter, external to the body, and the receiver, implanted into the body. [43] Figure 2.5 shows a block diagram of an inductive WPT.

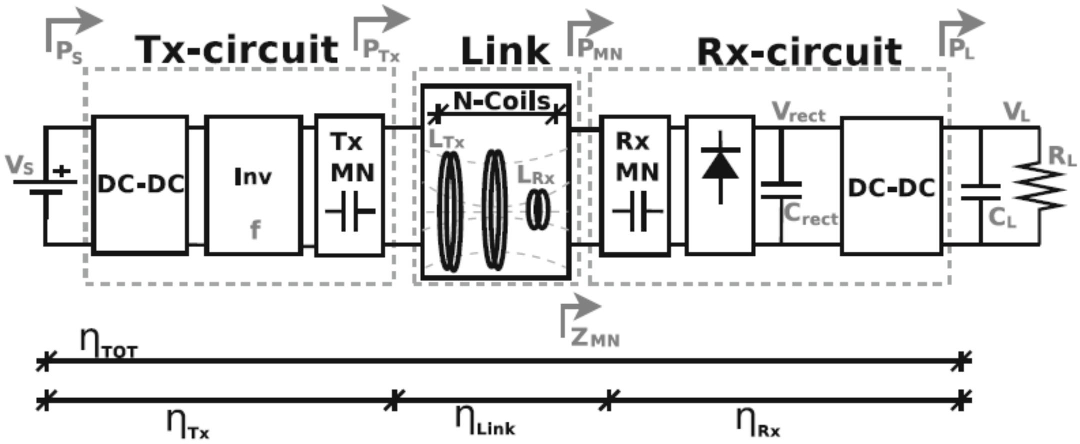

Figure 2.5. Block diagram of an inductive WPT system. [28]

The Transmitter Circuit (Tx-circuit) generates an alternating current in the Tx coil, labeled L_{TX}, which induces an alternating voltage in the Rx coil, labeled L_{RX}. The

Receiver Circuit (Rx-circuit) adapts this induced voltage to power the load, R_L.
The main parameters that define the WPT link are: [28]:

- the distance between Transmitter (Tx) and Receiver (Rx), and their relative orientation with respect to one another;
- the power carrier frequency, f;
- the Power Delivered to the Load P_L;
- Power Transfer Efficiency (PTE), η_{TOT}, defined as the P_L over the power taken from the primary power supply;
- Quality factor (Q) of a coil, defined as the ratio between its reactance ωL and its parasitic resistance R.

$$Q_{\text{Tx}} = \frac{\omega L_{\text{Tx}}}{R_{\text{Tx}}}, \quad Q_{\text{Rx}} = \frac{\omega L_{\text{Rx}}}{R_{\text{Rx}}}, \quad Q_L = \frac{\omega L_{\text{Rx}}}{\text{Re}\{Z_{\text{MN}}\}}, \quad Q_{\text{Rx-L}} = \frac{\omega L_{\text{Rx}}}{R_{\text{Rx}} + R_L}. \tag{2.4}$$

High-quality factors and high coupling coefficient are desired to reduce losses and increase η_{Link} under almost any condition. [28]
The receiving system, which is the main focus of this thesis project, is composed of four main blocks:

- **Inductive Link**: The inductive link basically works as a transformer, transferring the power through the magnetic field, which is alternating at the carrier frequency. [28]
- **RX matching network**: A matching network is usually implemented between the receiving coil and the rectifier to ensure that the impedance of the RX antenna matches the input impedance of the rectifier. [26] Impedance mismatch can lead to reflections, power losses, and reduced efficiency. Therefore, matching networks are essential components for maximizing power transfer. [26] In order to adapt the load impedance of the Rx coil with the rest of the inductive link, $Z_{MN_{\text{opt-}n}}$ was calculated. It represents the optimum value for Z_{MN} that maximizes the link efficiency η_{Link}. [28]

$$\text{Re}[Z_{MN_{\text{opt-}n}}] = R_{Rx}\sqrt{k^2_{Tx\text{-}Rx}\, Q_{Tx}\, Q_{Rx} + 1}$$

  Only the real part was considered, since the imaginary one is canceled by the resonant capacitor placed in series. [28]

- **RX rectifier**: A rectifier is required because the load circuit usually needs a DC voltage. Its design strongly depends on the operating frequency and power level structures. Regardless of the selected architecture, the goal is to rectify the input signal as efficiently as possible, minimizing power dissipation. [28]
- **DC-DC converter** : A DC-DC converter is placed after the rectifier to regulate its output voltage to the value required by the load. [28]

The design of each of these blocks will be illustrated in detail in Chapter 3.

2.3.3 Power Transfer Efficiency

Since there is no radiation in the near-field regime, the energy losses within the inductive link mainly occur in the parasitic resistances of the transmitter and receiver coils, denoted as R_{Tx} and R_{Rx}, respectively. Therefore, the power supplied by the transmitter circuit, P_{Tx}, is either transferred to the receiver circuit as P_{MN} or dissipated as heat in the coil resistances. [44]
The Power Transfer Efficiency (PTE) of the inductive link, denoted as η_{Link} and defined in Figure 2.5, is expressed as the ratio between the input power of the receiver circuit, P_{MN}, and the output power of the transmitter circuit, P_{Tx} [28]:

$$\eta_{\mathrm{Link}} = \frac{P_{\mathrm{MN}}}{P_{\mathrm{Tx}}}. \tag{2.5}$$

$$\eta_{\mathrm{Link}} = \underbrace{\frac{Q_{\mathrm{Rx\text{-}L}}}{Q_L}}_{\eta_{L_{\mathrm{Rx}}}} \underbrace{\frac{{k_{\mathrm{Tx\text{-}Rx}}}^2 Q_{\mathrm{Tx}} Q_{\mathrm{Rx\text{-}L}}}{{k_{\mathrm{Tx\text{-}Rx}}}^2 Q_{\mathrm{Tx}} Q_{\mathrm{Rx\text{-}L}} + 1}}_{\eta_{L_{\mathrm{Tx}}}}, \tag{2.6}$$

where $\eta_{L_{\mathrm{Rx}}}$ is the efficiency of the RX coil, defined as: [28]

$$\eta_{L_{\mathrm{Rx}}} = \frac{Q_{\mathrm{Rx}}}{Q_{\mathrm{Rx}} + Q_L} = \frac{Q_{\mathrm{Rx}\text{-}L}}{Q_L} \tag{2.7}$$

$\eta_{L_{\mathrm{Tx}}}$ is the efficiency of the Tx coil, defined as: [28]

$$\eta_{L_{\mathrm{Tx}}} = \frac{R_{\mathrm{Rx\text{-}Tx_{ref}}}}{R_{\mathrm{Rx\text{-}Tx_{ref}}} + R_{\mathrm{Tx}}} = \frac{k^2_{\mathrm{Tx\text{-}Rx}} Q_{\mathrm{Tx}} Q_{\mathrm{Rx}\text{-}L}}{k^2_{\mathrm{Tx\text{-}Rx}} Q_{\mathrm{Tx}} Q_{\mathrm{Rx}\text{-}L} + 1}. \tag{2.8}$$

Figure 2.6 shows the four main topologies of resonant coupling.

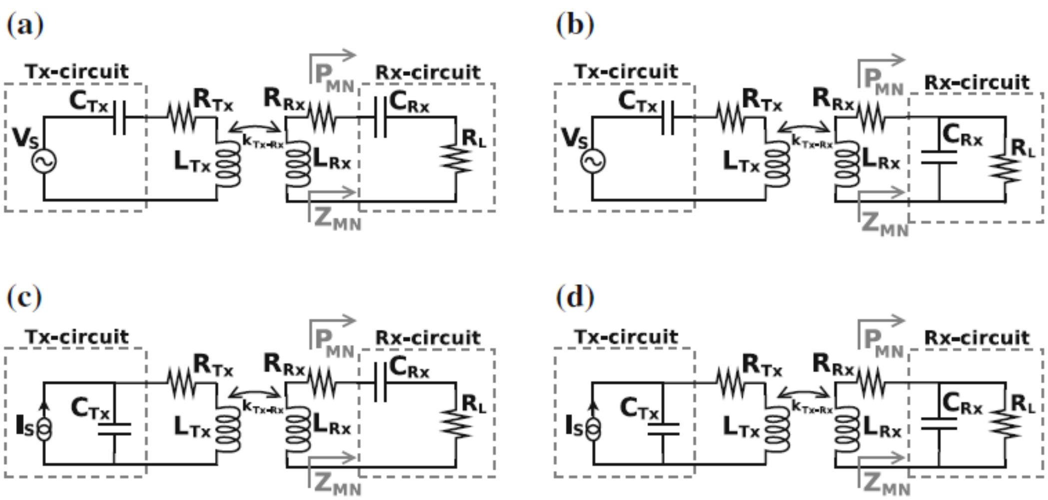

Figure 2.6. The four fundamental topologies of resonant coupling [28]

1. **Series-series:** typically used in high-power applications with a voltage source Tx. In this case, R_L and R_{Rx} have the same order of magnitude.[28]

2. **Series-parallel:** typically used in low-power applications with a voltage source Tx. In this case, R_L is much higher than R_{Rx}.[28]

3. **Parallel-series:** typically used in high-power applications with a current Tx source. In this case, R_L and R_{Rx} have the same order of magnitude.[28]

4. **Parallel-parallel:** typically used in low-power applications with a current Tx source. In this case, R_L is much higher than R_{Rx}.[28]

The Series-Series (SS) compensation topology was selected over all the configurations. It consists of series capacitors on Tx and Rx side. [32] These capacitors are then calibrated to resonate at the specific nominal frequency in 2.3:

$$\frac{1}{C_{Tx} \cdot \omega} = \omega \cdot L_{Tx} \tag{2.9}$$

$$\frac{1}{C_{Rx} \cdot \omega} = \omega \cdot L_{Rx} \tag{2.10}$$

Resonant condition allows to minimize the reactive power absorbed by the circuit and therefore to maximize the efficiency. [45]
The SS compensator is better tailored for the low-loaded applications and allows high efficiency even at low coupling coefficients. [45]. When the operating frequency is kept fixed at the resonant frequency, the SS topology can exhibit a nearly constant voltage gain over a limited range of coupling coefficients and load resistances. This behavior is due to the fact that the SS compensation keeps the link close to resonance, reducing the sensitivity of the voltage transfer to moderate variations of the inductive link and equivalent load. Similar dependencies of the voltage gain on mutual inductance, load and operating frequency in SS-compensated WPT systems are discussed in [46]. Compared to the SP topology, the SS compensator is explicitly better tailored for low-load applications, as it maintains a more reliable and higher voltage gain. [46]
This aspect also simplified the design of the following matching network, since at resonance the reactive components of the compensated inductive link are ideally canceled and the equivalent impedance becomes mainly resistive. A major theoretical and practical advantage is that the required transmitting side compensation capacitance C_{TX} depends entirely on the primary self-inductance and the resonant frequency. [46] As a result, the impedance transformation required by the matching network could be designed more directly. Moreover, the LTspice simulations performed during this work showed that the SS topology provided better performances than the SP topology under the considered low-power operating conditions. For these reasons, the SS compensation topology was selected for the receiver design.

2.4 Constraints for Biomedical Applications

2.4.1 Dimensions

In AIMDs, the physical size of the implanted receiver is one of the main design constraints. Since these devices must be placed inside the human body, the receiver should be as small as possible to reduce invasiveness and avoid interfering with the surrounding tissues and organs. Consequently, the receiving coil should also be minimized, as it usually represents one of the largest components of the implanted WPT system.

However, reducing the size of the receiving coil directly affects the inductive link performance. A smaller coil generally leads to a lower coupling coefficient, reducing the amount of power that can be transferred from the external transmitter to the implanted receiver. This becomes particularly critical when the implant is located deeper inside the body, when misalignment occurs, or when the device requires higher power levels. Therefore, the design of the Rx coil represents a key challenge in implantable WPT systems, since it requires a trade-off between the physical constraint of minimizing the implant size and the electrical requirement of ensuring sufficient coupling and transferred power.

2.4.2 Specific Adsorption Rate (SAR)

Exposure to RF is tightly limited by standards. It was observed by Mohanarangam et al. [47] that the Specific Adsorption Rate (SAR) value at low frequency is small when compared to high frequency irrespective of the shape of the coil. The maximum averaged SAR for the human head is set by the Federal Communications Commission (FCC) to 1.6 W/Kg for 1 g of tissue mass measured during 6 minutes of exposure. [42]
SAR is defined as:

$$\mathrm{SAR} = \frac{\sigma |E_{\mathrm{rms}}|^2}{\rho} \tag{2.11}$$

where E_{rms} is the magnitude of the electric field; σ and ρ are respectively the tissue conductivity and density. Following the Maxwell's equation, it is possible to extract the electric field E from the magnetic field B:

$$\nabla \times E = -\frac{\partial B}{\partial t} \propto 2\pi f_p I_1 \tag{2.12}$$

where f_p is the operating frequency and *I1* is the flowing current. Therefore, several environments for the exposure's simulation assumed that the SAR is proportional to $(\omega_p I_1)^2$. Since the electric field is proportional to the current and the frequency, it is possible to increase the external current while keeping constant the SAR by proportionally decreasing the operating frequency of the link. [42] It was proved by Mohanarangam et al. [47] that in an implantable coil, usually placed in 10 mm depth in human tissue, at 13.56 MHz in low-power applications, it is very unlikely for SAR to exceed the maximum value. [47]

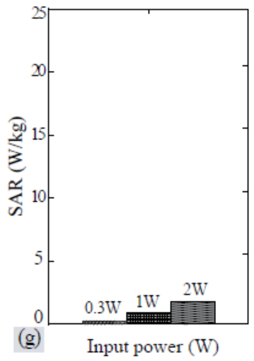

Figure 2.7. SAR vs. Input power at 13.56 MHz. [47]

Fig. 2.7 shows calculated SAR in a human tissue model formed using three consecutive layers of 1 mm skin, 2 mm fat and 7 mm muscle. At 13.56 MHz, for an input of 0.3 mW, SAR is 0.29. [47] The SAR cannot be measured experimentally and therefore it was measured with high frequency structure simulator (HFSS), simulating the system at 13.56 MHz. [47]

2.4.3 Overheating

Overheating is a common problem in WPT systems, particularly in NRIC systems: according to European Standard EN45502-1 [48], an implanted device's temperature must not rise more than 2°C over body temperature. The overheating is mainly due to the poor power transmission efficiency (PTE) and the low coil quality factor. Several factors, such as load variation, coil misalignments, and coil distance, influence the PTE. Poor PTE means that more power is lost as heat, which can cause the system to overheat, harming the surrounding human tissue. [49] The dissipated heat in both Tx and Rx coils should be strictly limited to prevent excessive temperature elevation, which may harm the surrounding human tissue. [28]

2.4.4 Coil Misalignment

One of the main challenges associated with NRIC is its high sensitivity to coil misalignment. [26] The PTE and the amount of power that may be transferred are consistently reduced by the axial and angular misalignment between magnetically connected coils. Coil misalignment reduces the magnetic coupling between the transmitter and receiver coils. As a consequence, the impedance reflected from the receiver side to the transmitter side decreases, modifying the effective load seen by the primary coil driver. This reduces the power transferred to the receiver and can move the transmitter away from its optimal operating condition, increasing switching losses and reducing the transmitter efficiency. Therefore, as misalignment increases, both the power delivered to the receiver and the overall link efficiency decrease [50].

- Vertical displacement: coils are aligned but their distance is changing.

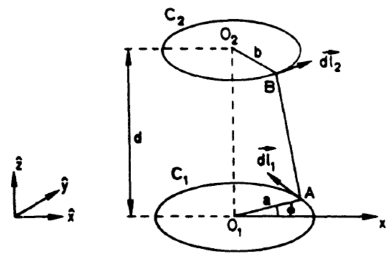

Figure 2.8. Vertical coil misalignment. [51]

- Lateral displacement: coils are placed in parallel planes but their centers are displaced by a distance Δ. [51]

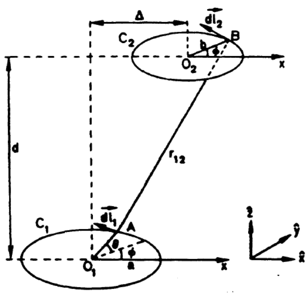

Figure 2.9. Lateral coil misalignment. [51]

- Angular displacement: the planes of the coils are tilted to form an angle a and the axis of one coil passes through the center of the other one. [51]

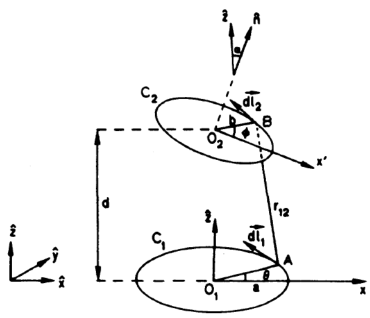

Figure 2.10. Angular coil misalignment. [51]

Experimental results for each misalignment will be presented in Chapter 6.

2.5 Receiver Requirements

In implantable electronic architectures, maximizing power transfer efficiency remains a key requirement. Inefficient power transfer can increase losses in the receiver and surrounding tissues, leading to local heating. Therefore, high efficiency is essential to limit temperature rise and ensure patient safety. The core challenge of the receiver design stems from the low power transmission levels. The electrical requirements diverge into two specific targets based on the destination project:

- **NerveRepack Configuration:** The receiving system must provide a highly stable dual-rail voltage supply of ± 3.3 V to the load.
- **Rewire Configuration:** The circuit must provide an expanded multi-rail compliance delivering $+3.3$ V, $+7$ V, and -7 V output rails to the load.

To limit energy dissipation in biological tissues while enabling efficient near-field magnetic coupling, the carrier frequency was set to the 13.56 MHz ISM band, as discussed in Section 2.3.2.
Since the heating constraint requires the tissue temperature rise to remain below 2°C, as explained in 2.4, a highly optimized power chain is necessary to minimize the dissipated heat fraction ($P_{\text{loss}} = P_{\text{IN}} - P_{\text{OUT}}$) generated by the rectifier and the subsequent DC/DC stages.
The physical positioning of the subcutaneous receiver circuit with respect to the external transmitter adds major electrical variables:

- Transcutaneous links are highly susceptible to angular and axial misalignments due to patient movement or placement tolerances. The system must operate reliably across an established nominal distance of 10 mm (1 cm);
- The input impedance of the rectifier changes non-linearly as the load power consumption shifts. The receiving matching network must be designed to transform the variable load into a target optimal impedance, preventing frequency splitting. In the frequency splitting phenomenon, the system loses its single Zero-Phase-Angle (ZPA) operating point and splits into two distinct peak frequencies, which severely destabilizes the voltage gain and degrades power transfer efficiency. [46];
- Footprint size must be minimized for active components, inductors and capacitors in order to maintain a layout footprint that can result in sufficiently low dimensions.

Chapter 3

Materials and Methods

3.1 Design of the receiving system

Two different boards were designed, following the different requirements of NerveRepack and Rewire projects. The RHS2116 requires different supply rails because its recording/-control circuitry and stimulation circuitry are powered by separate domains. The 3.3 V supply corresponds to V_{DD} and is required to power the digital logic, SPI interface, ADC, multiplexing circuitry, and amplifier stages. According to the datasheet [7], V_{DD} must be regulated between 3.2 V and 3.6 V, with 3.3 V as the recommended nominal value. In addition to V_{DD}, the stimulation circuitry requires two dedicated supply rails, $V_{\mathrm{STIM+}}$ and $V_{\mathrm{STIM-}}$. These rails define the compliance voltage available to the constant-current stimulators and allow the chip to generate biphasic stimulation pulses.
For the NerveRepack receiver, the stimulation rails were set to $V_{\mathrm{STIM+}} = +3.3\,\mathrm{V}$ and $V_{\mathrm{STIM-}} = -3.3\,\mathrm{V}$. This configuration reduces the required output power and is suitable for lower stimulation requirements. In the Rewire receiver, $V_{\mathrm{STIM+}} = +7\,\mathrm{V}$ and $V_{\mathrm{STIM-}} = -7\,\mathrm{V}$ were adopted, providing the maximum symmetric stimulation range allowed by the chip, equal to 14 V. This larger compliance range is required to support higher stimulation currents and more demanding electrode tissue loads. In the following chapter, the choices made for each block of the receiving circuit will be illustrated, according to the two project requirements.

3.1.1 Load

During the receiver design, it is essential to identify the power consumption of the target device, represented by The Intan Technologies RHS2116 microchip, a bidirectional electrophysiology interface system suitable for a wide variety of biopotential interfacing applications. [7] In particular, the current drawn from each supply rail must be evaluated in order to define equivalent load resistances that emulate the electrical behavior of the device. For this purpose, three different resistor values, R_{VDD} R_{VSTIM+}, R_{VSTIM-}, were calculated in order to simulate the load: R_{VDD} represents the resistor connected to the power supply (3.3V). R_{VSTIM+} represents the resistor connected to the positive stimulator power supply V_{STIM+}; R_{VSTIM-} represents the resistor connected to the negative stimulator power supply V_{STIM-};

The current contributions due to the quiescent and stimulation operating modes were separately evaluated and then combined to determine the total current consumption of each channel. First, the quiescent current drawn from the V_{DD} supply was calculated by summing the baseline current consumption in 3.1, the contribution of the AC amplifiers, the ADC current consumption, and the impedance monitoring circuitry contribution in [7]

VSTIM±	**supply current from VSTIM+**	**supply current from VSTIM–**
±3.3V	0.57 mA	0.41 mA
±7.0V	0.62 mA	0.48 mA

Table 3.1. Quiescent currents for supply levels of interest. [7]

$$I_{\text{AC}} = n_{\text{ch}} \cdot 9.2\,\mu\text{A/kHz} \cdot f_H \tag{3.1}$$

$$f_{\text{sample}} = n_{\text{ch}} \cdot f_{\text{sample,ch}} \tag{3.2}$$

$$I_{\text{ADC/MUX}} = 5.2\,\mu\text{A/(kS/s)} \cdot f_{\text{sample}} \tag{3.3}$$

$$I_{\text{imp}} = 0.12\,\text{mA} \tag{3.4}$$

The current related to stimulation consumption was then evaluated considering biphasic stimulation pulses, as shown in Figure 3.1.

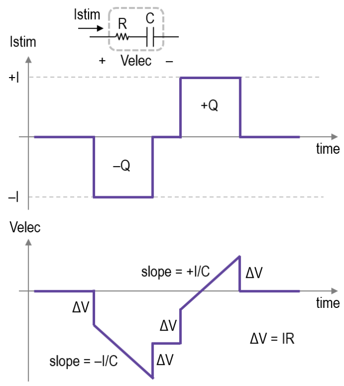

Figure 3.1. Typical biphasic current pulse, and a simplified series RC model of an electrode. [7]

Impulse width, T, values are in a range from T_{MIN} = 20 µs to T_{MAX} =1 ms.
The duty cycle of the stimulation signal was defined as:

$$D = f_{\text{stim}}(T_1 + T_2) \tag{3.5}$$

where f_{STIM} is the stimulation frequency, while T1 and T2 represent the durations of the negative and positive stimulation phases, respectively.
The instantaneous currents for the positive and negative stimulation phases were converted into average current values through a time weighted averaging procedure.
If a positive stimulation current with magnitude I_{STIM} is supplied from one channel, the currents drawn from each power supply increase during stimulation as follow: [7]

$$V_{DD} \quad \Delta I = 0.23 \cdot I_{\mathrm{STIM}} \tag{3.6}$$
$$V_{STIM+} \quad \Delta I = 1.15 \cdot I_{\mathrm{STIM}} \tag{3.7}$$
$$V_{STIM-} \quad \Delta I = 0 \tag{3.8}$$

If a negative stimulation current is supplied from one channel, the current increases by the stimulation:

$$V_{DD} \quad \Delta I = 0.10 \cdot I_{\mathrm{STIM}} \tag{3.9}$$
$$V_{STIM+} \quad \Delta I = 0.34 \cdot I_{\mathrm{STIM}} \tag{3.10}$$
$$V_{STIM-} \quad \Delta I = 1.31 \cdot I_{\mathrm{STIM}} \tag{3.11}$$

I_{STIM} values are in a range from $I_{\mathrm{STIM,\ MIN}} = 2.55$ µA to $I_{\mathrm{STIM,\ MAX}} = 2.5$mA, according to [7].
The average stimulation current was therefore obtained as:

$$I_{\mathrm{avg}} = \frac{T_1}{T_1 + T_2} I_{\mathrm{neg}} + \frac{T_2}{T_1 + T_2} I_{\mathrm{pos}} \tag{3.12}$$

The resulting average value was subsequently multiplied by the duty cycle in order to account for the pulsed operation of the stimulator.
The total current drawn from each supply rail was then calculated by summing the contributions of the quiescent and stimulation currents. Once the total currents were obtained, the overall power consumption of the system was calculated as:

$$P_{\mathrm{tot}} = V_{DD} I_{VDD,\mathrm{tot}} + V_{STIM} I_{VSTIM+,\mathrm{tot}} + V_{STIM} I_{VSTIM-,\mathrm{tot}} \tag{3.13}$$

Different parameters were used for NerveRepack and Rewire projects, as shown in Table 3.2.

Parameter	**NerveRepack**	**Rewire**
ch_{stim}	2	8
ch_{rec}	5	8
V_{stim}	3.3 V	7 V
f_H	5 kHz	10 kHz
$f_{\mathrm{sample,ch}}$	10 kS/s/channel	20 kS/s/channel

Table 3.2. Comparison of the main system parameters for the NerveRepack and Rewire projects

Different studies including RHS2116 were considered [52, 53, 54, 55], and summarized in Table 3.3.

Article	Waveform	Frequency (f)	Pulse Width
Wright et al.	Biphasic, charge-balanced waveform with passive charge balancing	30 Hz	1000 μs (range: 100–1000 μs)
Lienemann et al.	Biphasic pulse trains, cathodic-first	1 Hz	200 μs
Zurita et al.	Bipolar, charge-balanced pulse trains	1 Hz	500 μs
Carnicer-Lombarte et al.	Trains of 100 biphasic pulses	100 Hz (10 ms period)	100 μs

Table 3.3. Comparison of stimulation parameters reported in selected neural interface studies.

$f_{STIM} = 30Hz$ was chosen, to evaluate the worst case. [52].
Figures 3.2 and 3.3 show the power calculation results for the two projects.

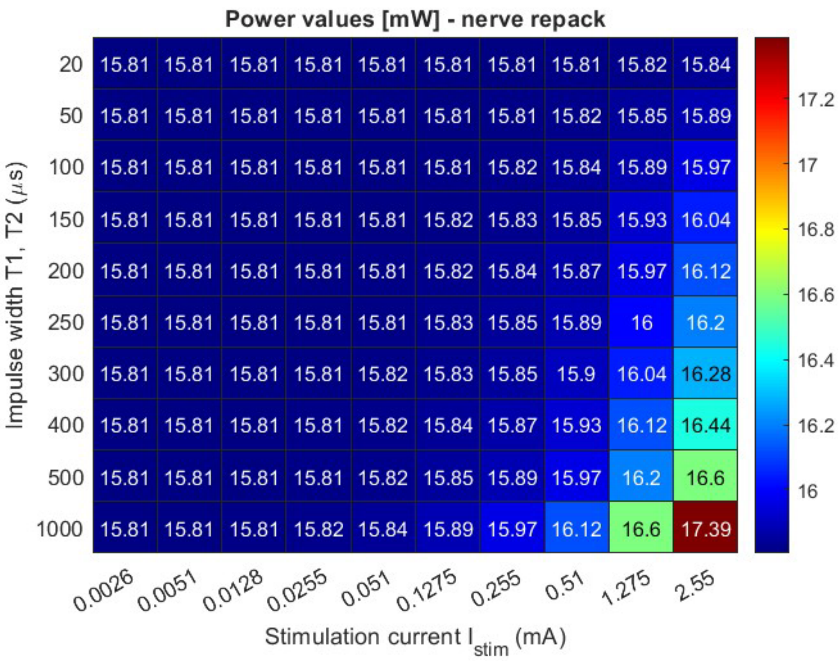

Figure 3.2. Estimated power consumption for the NerveRepack circuit.

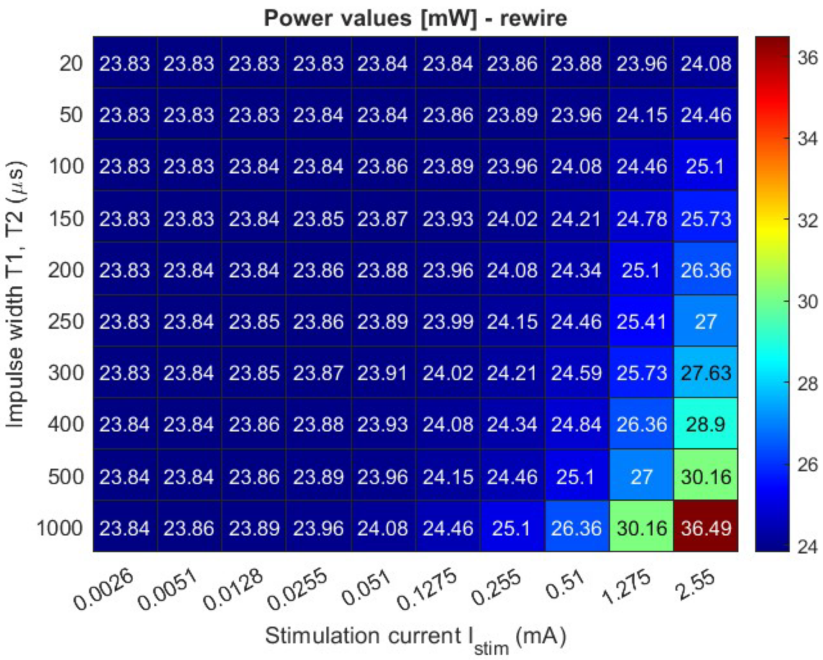

Figure 3.3. Estimated power consumption for the Rewire circuit.

The color scale and the numerical values inside each cell represent the total power expressed in mW. The lower power values, highlighted in blue and approximately equal to 16 mW, and 24 mW represent the standard operating condition. The maximum power consumption is equal to $P_{\mathrm{MAX}} = 17.39\,\mathrm{mW}$ for NerveRepack and $P_{\mathrm{MAX}} = 36.49\,\mathrm{mW}$ for Rewire. These maximum power conditions, corresponding to the highest stimulation current and pulse width ($I_{\mathrm{STIM}} = 2.55\,\mathrm{mA}$ and $T_1 = T_2 = 1000\,\mu\mathrm{s}$), were used to evaluate the equivalent resistance values in MATLAB, by using the following equations:

$$R_{\mathrm{vdd}} = \frac{V_{\mathrm{dd}}}{I_{\mathrm{vdd,tot}}} \tag{3.14}$$

$$R_{\mathrm{vstim+}} = \frac{V_{\mathrm{stim}}}{I_{\mathrm{vstim+,tot}}} \tag{3.15}$$

$$R_{\mathrm{vstim-}} = \frac{V_{\mathrm{stim}}}{I_{\mathrm{vstim-,tot}}} \tag{3.16}$$

Parameter	**NerveRepack**	**Rewire**
R_{VDD}	854.81 Ω	648.34 Ω
R_{VSTIM+}	4135.49 Ω	4569.55 Ω
R_{VSTIM-}	5406.03 Ω	5461.41 Ω

Table 3.4. Equivalent load resistances for the NerveRepack and Rewire systems

Given these resistance values,

$$R_{\text{target}} = \frac{P_{\max}}{P_{\text{target}}} R_{\max} \tag{3.17}$$

Where P_{max} is the maximum power value showed in Figures 3.2 and 3.3, R_{meas} are the measured resistance values in 3.4 and P_{target} are the output values considered for circuit efficiency evaluations in simulation, respectively 16 mW, 30 mW, 50 mW, 100 mW for NerveRepack and 24 mW, 30 mW, 50 mW, 100 mW for Rewire.

Load power	R_{VDD} [Ω]	R_{VSTIM+} [Ω]	R_{VSTIM-} [Ω]
16 mW	929.00	4494.76	5875.65
30 mW	494.40	2394.00	3120.00
50 mW	297.20	1438.30	1880.00
100 mW	148.65	719.16	940.10

Table 3.5. Load resistance configurations for the NerveRepack receiver.

Load power	R_{VDD} [Ω]	R_{VSTIM+} [Ω]	R_{VSTIM-} [Ω]
24 mW	985.73	6947.6	8301.34
30 mW	788.59	5558	6642.89
50 mW	473.15	3335	3986
100 mW	236.57	1667.52	1993

Table 3.6. Load resistance configurations for the Rewire receiver.

3.1.2 DC/DC Converters

DC/DC converters were selected to generate the regulated supply voltages required by the two receiver circuits. Since a stable 3.3 V supply must be provided in both architectures, the same converter, the LTC3129-1 from Analog Devices, was adopted for V_{DD}.
In the NerveRepack receiver, the LTC660 was employed to obtain the negative −3.3 V rail, whereas the LT3471 was selected to generate the +7 V and −7 V stimulation supply rails in the Rewire receiver.

LTC3129-1

The LTC3129-1 is a high-efficiency, 200 mA buck-boost DC/DC converter with a input range from 2.42V to 15V and output voltage range from 2.5V to 15V. [56] In this work, the output voltage was configured to $V_{\text{OUT}} = 3.3\,\text{V}$ according to the pin configuration reported in Table 3.7.
VS3 and VS2 were connected to ground, while VS1 pin was connected to VCC. The adopted configuration is shown in Figure 3.4 [56].

VS3 PIN	VS2 PIN	VS1 PIN	VOUT
0	0	0	2.5V
0	0	V_{CC}	3.3V
0	V_{CC}	0	4.1V
0	V_{CC}	V_{CC}	5V
V_{CC}	0	0	6.9V
V_{CC}	0	V_{CC}	8.2V
V_{CC}	V_{CC}	0	12V
V_{CC}	V_{CC}	V_{CC}	15V

Table 3.7. Vout Program Settings. [56]

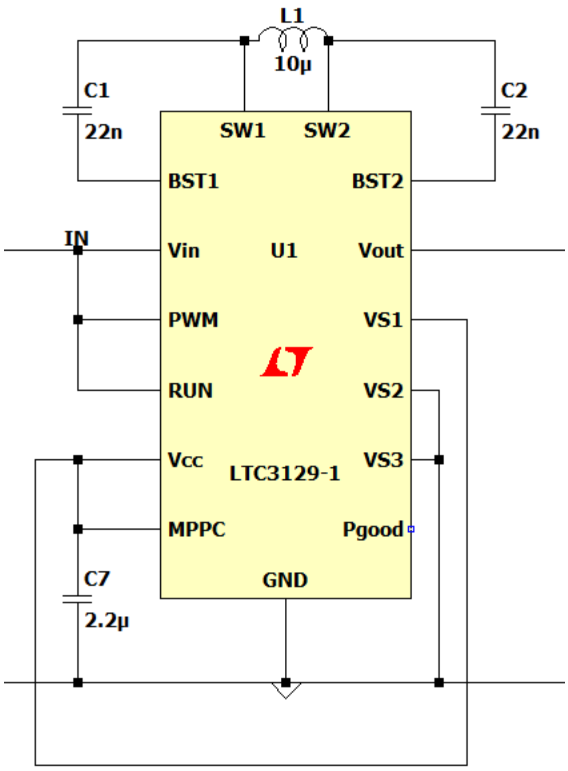

Figure 3.4. LTC3129-1 LTSpice configuration

LTC660

In the NerveRepack receiver, the LTC660 was used in voltage-inverting configuration to generate the negative stimulation rail. Its configuration in LTSpice is shown in Figure 3.5. In particular, the +3.3 V supply was converted into −3.3 V, providing the required

$V_{\mathrm{STIM}-}$ voltage for the RHS2116 chip. The LTC660 is a monolithic CMOS switched-capacitor voltage converter. It can operate as a voltage inverter, converting a positive input supply into a complementary negative output voltage. For this operating mode, the input voltage range is from 1.5 V to 5.5 V, resulting in output voltages from −1.5 V to −5.5 V. The device can also be configured as a voltage doubler, with an input voltage range from 2.5 V to 5.5 V and a corresponding output voltage from 5 V to 11 V [57].

The use of a switched-capacitor converter is particularly suitable for this receiver because it allows the negative rail to be generated without using an inductor. This reduces the number of magnetic components on the PCB, which is an advantage in terms of size reduction and layout simplicity. Moreover, since the negative rail in the NerveRepack architecture is limited to −3.3 V, the LTC660 can directly generate the required $V_{\mathrm{STIM}-}$ voltage starting from the available +3.3 V rail.

Switched-capacitor converters are generally more suitable for low-current applications, since their output voltage decreases as the load current increases due to the equivalent output resistance of the charge pump stage. [58]

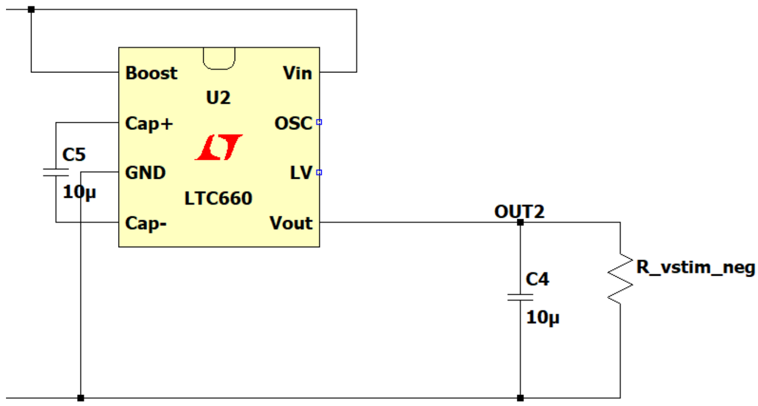

Figure 3.5. LTC660 SPICE configuration

LT3471

In the Rewire receiver, the stimulation circuitry requires two higher voltage rails: $V_{\mathrm{STIM}+} = +7\,\mathrm{V}$ and $V_{\mathrm{STIM}-} = -7\,\mathrm{V}$. For this reason, the LT3471 from Analog Devices was selected. The LT3471 is a dual switching regulator that includes two internal power switches, each rated for a maximum voltage of 42 V and current of 1.3 A, and two error amplifiers. This architecture allows the device to be configured both as a non-inverting boost converter and as an inverting converter [59]. The LT3471 was selected because it can generate both the positive and negative stimulation rails using a single integrated device. This is particularly useful in the proposed architecture. Compared to the NerveRepack receiver, the Rewire configuration requires higher stimulation voltages and a larger available output power; therefore, an inductive switching regulator is more suitable than a switched-capacitor converter. On the other hand, the architecture requires higher number of required external components, including inductors, diodes, feedback resistors, and compensation components. One output was configured to generate the positive stimulation rail, $V_{\mathrm{STIM}+} = +7\,\mathrm{V}$, while the other output was configured to generate the negative stimulation rail, $V_{\mathrm{STIM}-} = -7\,\mathrm{V}$, as shown in Figure 3.6.

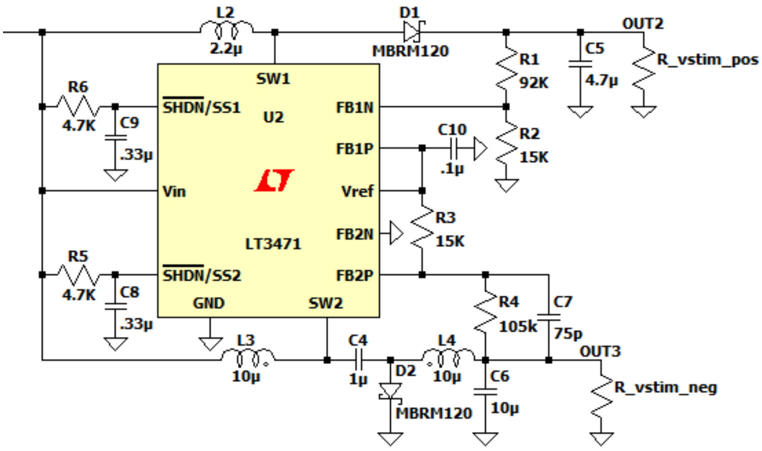

Figure 3.6. LT3471 SPICE architecture

For the non-inverting boost output, the output voltage is set by the feedback resistor divider according to [59]:

$$V_{\mathrm{OUT2}} = V_{\mathrm{FBP}} \left(1 + \frac{R_1}{R_2}\right) \tag{3.18}$$

Therefore, the upper feedback resistor can be calculated as:

$$R_1 = R_2 \left(\frac{V_{\mathrm{OUT2}}}{V_{\mathrm{FBP}}} - 1\right). \tag{3.19}$$

Since V_{FBP} is tied to the internal reference voltage, $V_{\mathrm{REF}} = 1.00\,\mathrm{V}$, and R_2 was set to the typical value of $15\,\mathrm{k\Omega}$, the current flowing in the feedback divider is approximately:

$$I_{\mathrm{div}} = \frac{1.00\,\mathrm{V}}{15\,\mathrm{k\Omega}} \simeq 67\,\mu\mathrm{A}. \tag{3.20}$$

For the target output voltage $V_{\mathrm{OUT2}} = V_{\mathrm{STIM}+} = 7\,\mathrm{V}$, Equation 3.19 gives:

$$R_1 = 15\,\mathrm{k\Omega} \left(\frac{7}{1} - 1\right) = 90\,\mathrm{k\Omega}. \tag{3.21}$$

A standard resistor value close to this result was then selected.
For the inverting output, $V_{\mathrm{OUT3}} = -7\,\mathrm{V}$, the feedback network is configured with V_{FBN} tied to ground. The resistor R_3 is connected between V_{FBP} and V_{REF}, while R_4 is connected between V_{FBP} and V_{OUT3}. The output voltage is given by [59]:

$$V_{\mathrm{OUT3}} = -V_{\mathrm{REF}} \left(\frac{R_4}{R_3} \right). \tag{3.22}$$

As for the positive output, R_3 was set to $15\,\mathrm{k\Omega}$, resulting in a divider current of approximately $67\,\mu\mathrm{A}$. For the target voltage $V_{\mathrm{OUT3}} = V_{\mathrm{STIM-}} = -7\,\mathrm{V}$, Equation 3.22 gives:

3.1.3 Coil measurements

Figure 3.7 shows the transmitter coil, and Table 3.8 its geometrical values.

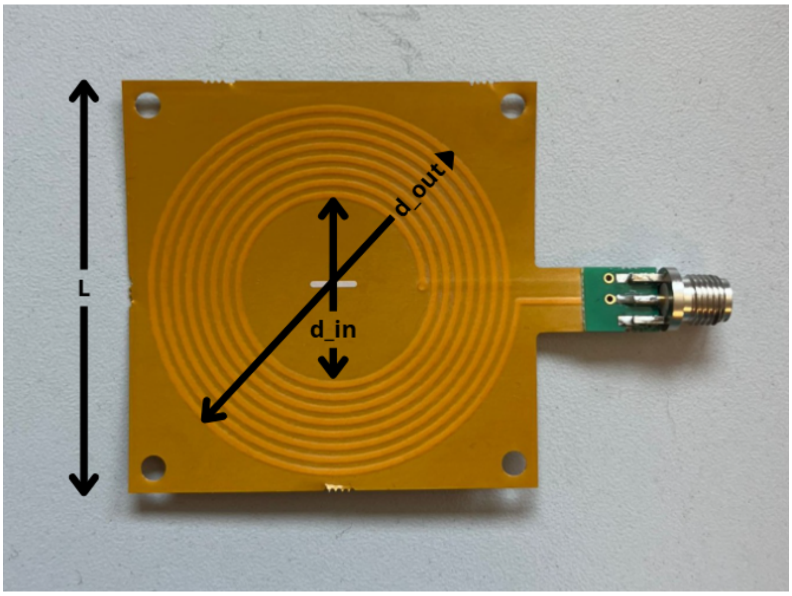

Figure 3.7. Transmitter Coil

L (mm)	d_in (mm)	d_out (mm)	w (mm)	s (mm)	N
50	21	46	0.75	0.75	8

Table 3.8. TX geometrical values

Figure 3.8 shows the receiver coil, and Table 3.9 its geometrical values.

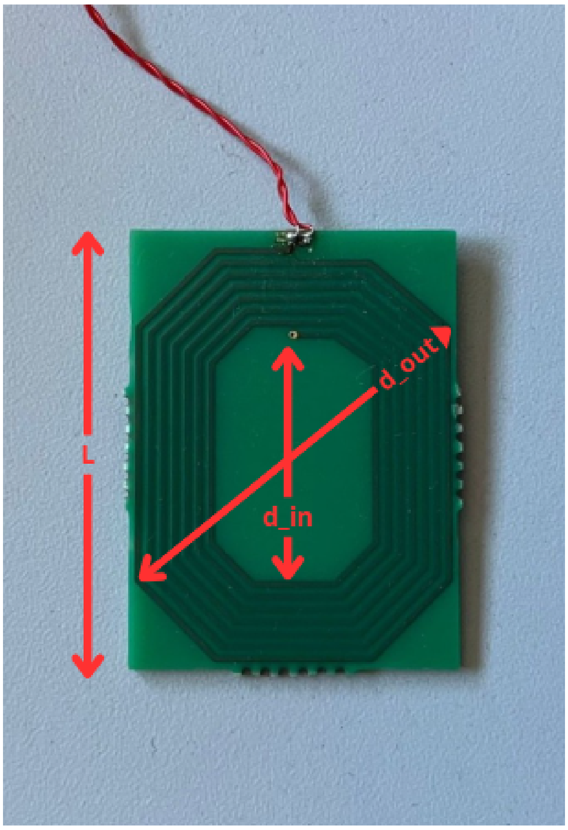

Figure 3.8. Receiver Coil

L (mm)	**d_in (mm)**	**d_out (mm)**	**w (mm)**	**s (mm)**	**N**
45	26	42	0.8	0.7	7

Table 3.9. RX geometrical values

Coil measurements were performed by using the Vector Network Analyzer (VNA) by Keysight in order to measure inductance and resistance values. An initial phase of electronic calibration was performed, enabling the VNA to factor out the effects of cables and adaptors used in the connection of the Device Under Test (DUT). [60]. Subsequently, measurements were performed at the operating frequency of 13.56 MHz in order to characterize the inductive link. The two cables, connected respectively to Port 1 and Port 2, were connected to the flexible transmitter coil and the receiver coil, to measure phase and magnitude of S_{11}, S_{21}, S_{12}, S_{22}. The separation distance between the two coils was set to 10 mm, a target separation distance to simulate biological tissues, including skin and subcutaneous fat, as shown in Fig. 3.9.

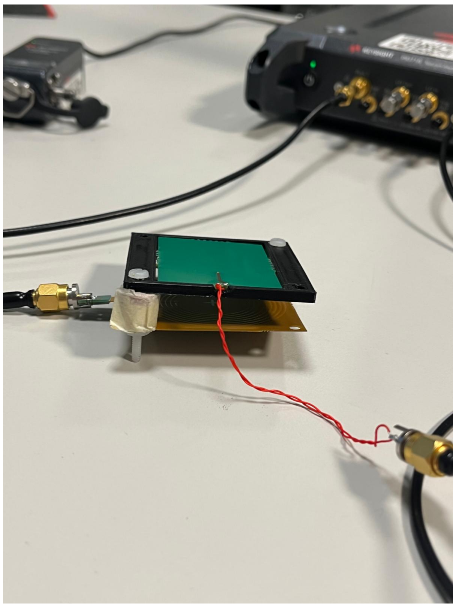

Figure 3.9. Measurements setup

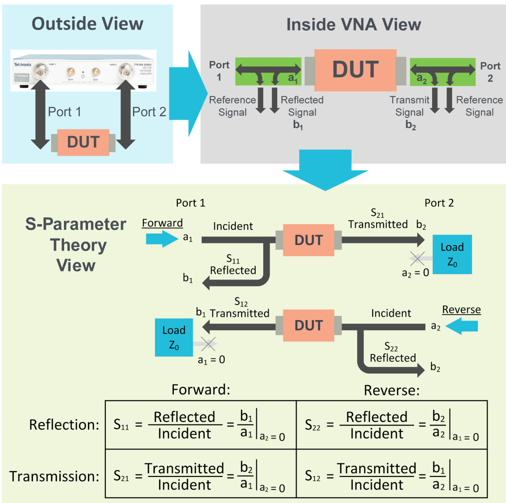

Figure 3.10. Understanding scattering parameters [60]

High frequency multiport networks are characterized by analyzing incident (a_n) and reflected (b_n) power wave phasors. For a two port network, the relationship between these waves is defined by the scattering matrix:

$$b_1 = S_{11}a_1 + S_{12}a_2$$

$$b_2 = S_{21}a_1 + S_{22}a_2$$

. A VNA measures these parameters using internal directional couplers to isolate the reference, incident, and reflected signals across two sequential operating modes:

- Forward Case ($a_2 = 0$): Port 1 transmits the stimulus (a_1) while Port 2 is terminated into a matched load (Z_0). This configuration yields the input reflection coefficient $S_{11} = b_1/a_1$ and the forward transmission coefficient $S_{21} = b_2/a_1$.
- Reverse Case ($a_1 = 0$): Port 2 transmits the stimulus (a_2) while Port 1 is matched. This allows measurement of the output reflection coefficient $S_{22} = b_2/a_2$ and the reverse transmission coefficient $S_{12} = b_1/a_2$.

Through this dual-stage measurement, the VNA fully determines the vector scattering matrix of the DUT. Throughout a MATLAB code, L and R values were extracted from S-parameters.

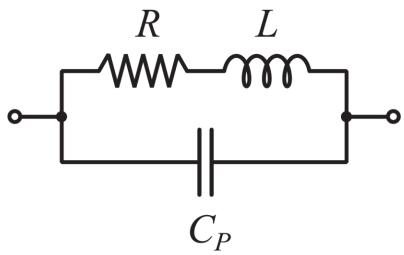

Figure 3.11. WPT coil electric model. [61]

The VNA measurements provide the scattering parameters over frequency. After conversion into impedance parameters, the magnitude and phase of the impedance can be used to extract the equivalent inductance, resistance, and impedance through the following equations: [43]

$$R = \Re(Z) = |Z| \cos\phi \tag{3.23}$$

$$X = \Im(Z) = |Z| \sin\phi \tag{3.24}$$

$$L = \frac{\Im(Z)}{2\pi f} \tag{3.25}$$

	L [H]	**R [Ω]**	**Q**
Transmitter coil	2.8e-6	6.33	37.33
Receiver coil	2.32e-6	6.03	32.8

Table 3.10. Electrical parameters of the transmitter and receiver coils

The coupling coefficient k was also calculated from the mutual inductance M and the self-inductances of the transmitter and receiver coils, L_1 and L_2, according to 2.2. The resulting coupling coefficient was equal to $k = 0.25$.

3.1.4 Rectifier

Three rectifier topologies were investigated: a voltage-doubler rectifier, a full-bridge rectifier, and a class-E rectifier.

Voltage doubler rectifier

Voltage doubler rectifiers are commonly used when a higher DC output voltage is required from an AC or RF input signal. The Greinacher voltage doubler, shown in Figure 3.12, represents one of the most widely adopted topologies in RF energy-harvesting. This architecture uses diodes and capacitors to both rectify the input waveform and increase the resulting DC output voltage. [62]

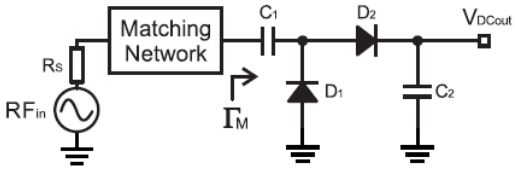

Figure 3.12. Greinacher voltage doubler topology

Full bridge topology

The full-bridge topology is widely used in power electronics and can be implemented with either diodes or active switches, such as power MOSFETs. When active switches are utilized, the full bridge rectifier is known as a synchronous rectifier. This configuration has been employed in inductive power transfer (IPT) systems for bidirectional power transfer, a feature that conventional diode bridge rectifiers have yet to achieve. However, this topology is not suitable for power transfer at MHz frequencies due to the challenging dead-time requirements for driving a full bridge at such high frequencies. Additionally, the overall electromagnetic interference (EMI) performance is negatively impacted at these frequencies. [63]

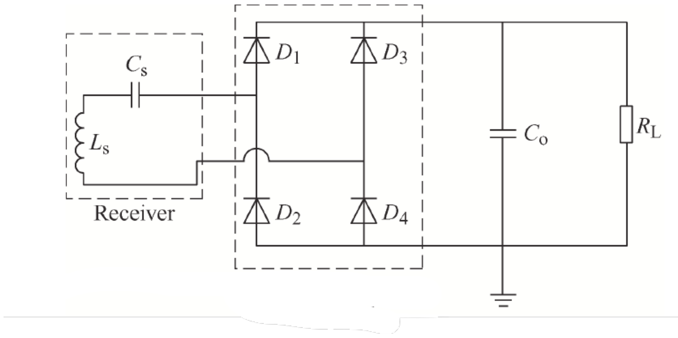

Figure 3.13. Full bridge topology. [63]

Class-E topology

Figure 3.14 illustrates a half bridge rectifier of the Class E type, which operates using a current-driven approach. The capacitor C_D connected across diode acts as a voltage snubber, enabling zero-voltage switching (ZVS) during turn on. The diode and capacitor are arranged in parallel with the second-order LC filter and the current-driven source. As a result, the current flowing through them is the combination of the AC current entering the system and the steady-state output current. [63]

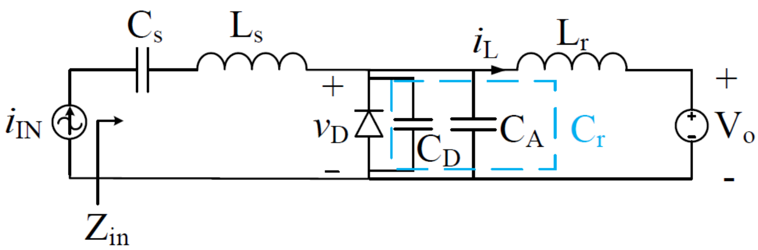

Figure 3.14. Class-E rectifier driven by a current source. [64]

Resonant rectifiers are included in power conversion systems operating at frequencies above 10 MHz. Applications for these circuits include very high frequency DC/DC converters, wireless power transfer systems. The design of the class-E rectifier begins with maximum output power $P_{o,\max}$, dc output voltage, V_0, frequency f, and diode peak voltage $V_{D,pk}$ specifications, [64] defined in Table 3.11.

Parameter	Value
$P_{o,\max}$	150 mW
V_o	6 V
$V_{D,pk}$	16 V
f	13.56 MHz

Table 3.11. Class E rectifier specifications

An ideal diode was used to simulate $V_{D,pk}$, the ideal peak voltage value used for the calculations. A diode MMBD452 [65] with a $V_{D,pk} = 30V$ was then chosen, to avoid the breakdown of the diode.

$$V_{D,n} = \frac{V_{D,pk}}{V_o} \tag{3.26}$$

where $V_{D,pk}$ is the diode peak reverse voltage

$$C_n = C_r \frac{2\pi f V_o^2}{P_{o,\max}} \tag{3.27}$$

$$L_n = L_r \frac{2\pi f P_{o,\max}}{V_o^2} \tag{3.28}$$

where $P_{o,\max}$ is the maximum rated output power.

After calculating $V_{D,n}$, normalized capacitance value was extracted in Fig. 3.15.

Through Cn value, Ln was extracted in Figure 3.16. By knowing Cn and Ln, Cr was calculated by 3.27 and Lr was calculated by 3.28. Considering Cr as the parallel between C_D and C_A, C_R cannot be chosen to be smaller than the intrinsic capacitance of the diode. [64]

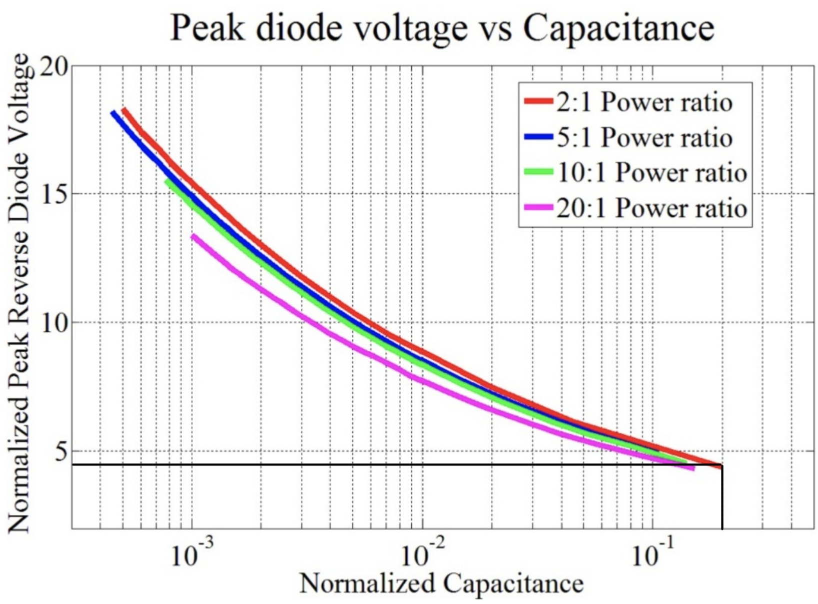

Figure 3.15. Maximum normalized peak diode voltage vs. normalized capacitance for different power range ratios ($P_{o,\max}$:$P_{o,\min}$). [64]

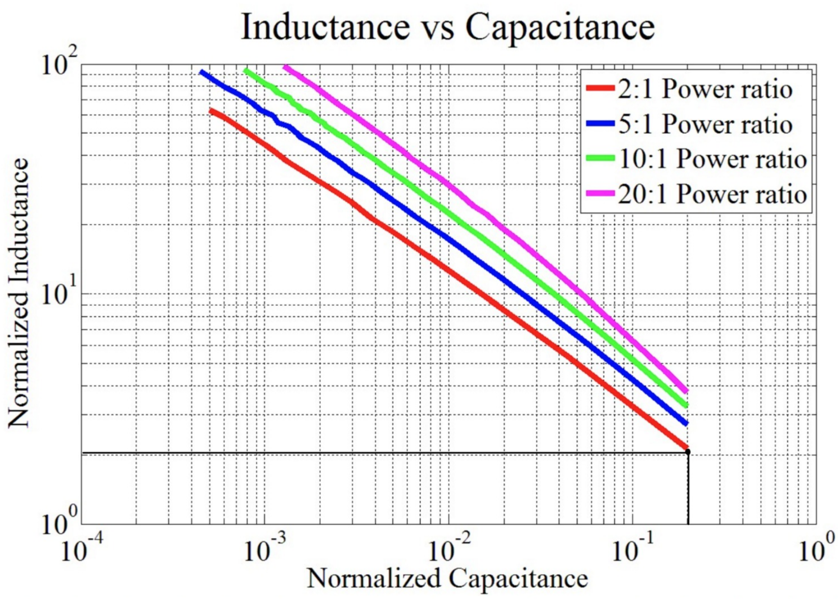

Figure 3.16. Normalized inductance vs. normalized capacitance for different power ranges ratios ($P_{o,\max}$:$P_{o,\max}$). [64]

Parameter	Value
C_n	0.2
L_n	2.01
C_r	9.78 pF
C_D	1.5 pF

Table 3.12. Class E rectifier design values

The *power range ratio* is a design parameter to define the operating power interval of the rectifier. It is defined as the ratio between the maximum rated output power, $P_{o,\max}$, and the minimum rated output power, $P_{o,\min}$, for which the rectifier is expected to operate correctly:

$$\text{Power Range Ratio} = \frac{P_{o,\max}}{P_{o,\min}}. \tag{3.29}$$

This parameter represents the variation of the equivalent load connected to the rectifier under normal operating conditions. In the rectifier design procedure, it is also useful to evaluate whether the input impedance remains mainly resistive over the selected power range.

Common values used for the power range ratio are:

- 2 : 1 corresponds to a small power variation;
- 5 : 1 corresponds to a moderate power variation;
- 10 : 1 corresponds to a wide power variation;
- 20 : 1 corresponds to a very wide power variation.

In this work, a 2 : 1 power range ratio was selected in order to evaluate the rectifier performance under a limited variation of the output load condition. This choice allows the rectifier to be optimized around the nominal operating point while still considering a realistic variation of the delivered power.

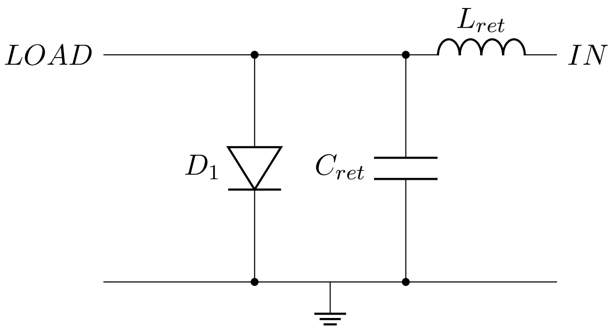

Parameter	Value
D_1	MMBD301LT1G
C_{ret}	8.28 pF
L_{ret}	5.9 μH

Figure 3.17. Class-E rectifier circuit and component values.

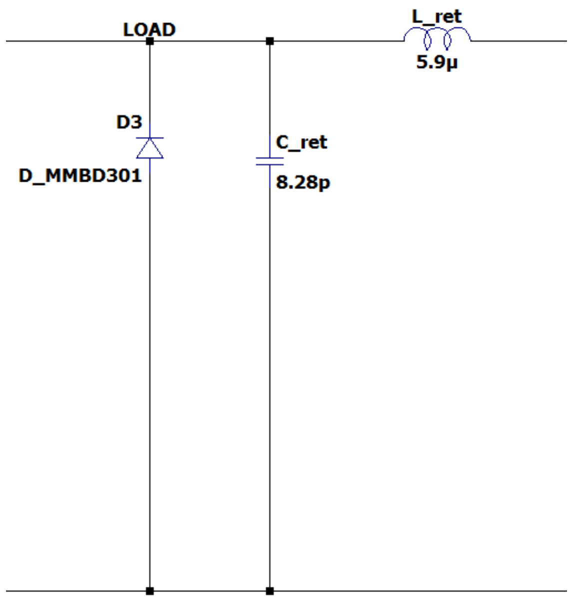

Figure 3.18. Class-E rectifier design in LTSpice

To compare the different rectifier topologies, SPICE simulations were performed by modeling the input of the following DC/DC converter stage as an equivalent resistive load to evaluate the efficiencies. The value of the equivalent resistance was calculated from the minimum input voltage required by the LTC3129-1, equal to $V_{\min} = 2.42\,\mathrm{V}$ [56] and from the corresponding input current:

$$R_{\text{eq}} = \frac{V_{\text{min}}}{I_{\text{input}}}. \tag{3.30}$$

This resistor was connected to the output of the rectifier. Then, an AC voltage or current source was placed at the rectifier input and its amplitude was adjusted until the average output voltage across the equivalent load reached at least 2.42 V. In this way, each rectifier topology was tested under the same minimum voltage requirement imposed by the DC/DC converter stage.
The average input and output powers were then calculated, and the rectification efficiency was evaluated as:

$$\eta_{\text{rect}} = \frac{P_{\text{out,avg}}}{P_{\text{in,avg}}} \cdot 100. \tag{3.31}$$

Table 3.13 reports the average input power $P_{\text{out,avg}}$, average output power $P_{\text{in,avg}}$, and rectification efficiency η_{rect} for the three rectifier topologies.

Rectifier topology	$P_{\text{out,avg}}$ **[mW]**	$P_{\text{in,avg}}$ **[mW]**	η_{rect} **[%]**
Class-E rectifier	43.33	52.21	83.00
Full-bridge rectifier	41.80	57.87	72.24
Voltage doubler	53.23	102.92	51.72

Table 3.13. Comparison of the simulated rectifier topologies.

Among the tested topologies, the class-E rectifier was selected because it provided the highest simulated efficiency over the considered operating range.

3.1.5 Matching Network

In order to match the $Z_{MN_{\text{opt}}}$ with the input rectifier impedance, different matching networks can be implemented including: T-Match, L-Match and π-Match [28], respectively a) b) and c) in 3.19.

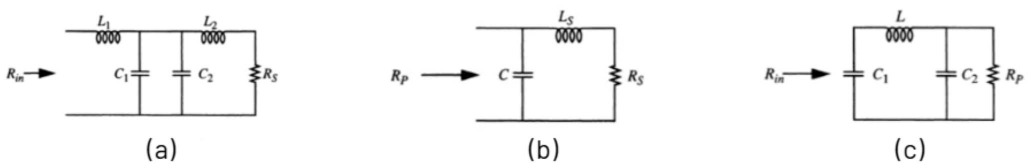

Figure 3.19. Matching Network typologies. [66]

The simplest form of LC matching networks, L-networks was used. The circuit consists of one inductor and one capacitor forming an L-shape. They are used for narrowband applications where the bandwidth is limited, offering simplicity and ease of design. Depending

on the configuration, they can transform higher to lower impedances or viceversa. LC matching networks are employed in RF amplifiers to maximize power transfer and minimize reflections between the amplifier stages and load. A mismatch between the load and source impedances in RF and high-frequency systems leads to reflections, reduced power transfer, and potential signal integrity issues. The ideal scenario is when both source and load have the same impedance, typically 50 Ω in many RF applications. Achieving that perfect match often requires adding reactive components—inductors and capacitors—in different configurations. The L matching network is adopted since it stands out for its simplicity and versatility. [67]
On the other hand, the L-match provides the lowest Q among matching networks and there is no freedom to arbitrarily set the bandwidth. Indeed, it only depends on R_L, resistance value that models the load circuit, and R_S, source resistance: [68]

$$Q = \sqrt{\frac{R_L}{R_S} - 1} \tag{3.32}$$

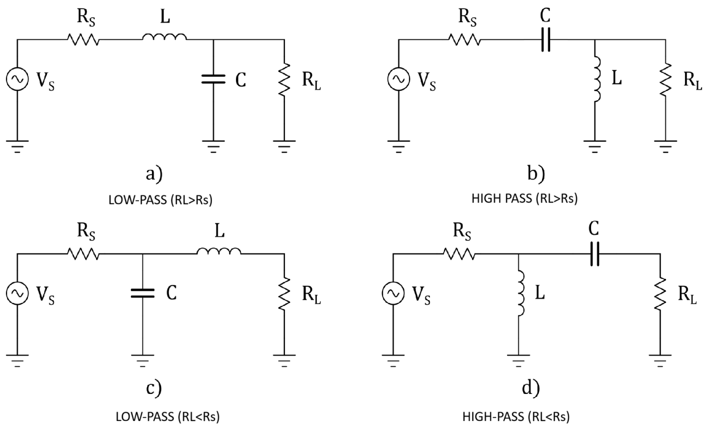

Figure 3.20. L-match configurations

As shown in Figure 3.20, an L-matching network can be used either to increase or decrease the impedance seen by the source, depending on its orientation. In general, the shunt element is placed on the side with the higher resistance. [68].
Therefore, the following design rules can be applied:

- if $R_L > R_S$, the shunt element is connected on the load side;
- if $R_L < R_S$, the shunt element is connected on the source side.

In this work, since $R_L > R_S$, the low-pass configuration (a) shown in Figure 3.20 was adopted.
LTSpice simulations were performed to validate and refine the matching network design. Although the same rectifier topology was used, its input impedance is not constant. Even

under the same load condition, the impedance seen at the rectifier input can change because of the nonlinear behavior of the rectifier. Therefore, the matching components were obtained through an iterative procedure. Through the Fourier analysis (.FOUR) provided by LTspice at the operating frequency of 13.56 MHz, the magnitude and phase of the fundamental harmonics were extracted for the input matching network voltage V_{MN}, the receiver capacitive current $I(C_{\text{rx}})$, the output voltage V_{LOAD}, and output current $I(V_{\text{im}})$ were converted into their corresponding complex phasors. All these points of interest are shown in Figure 3.21.

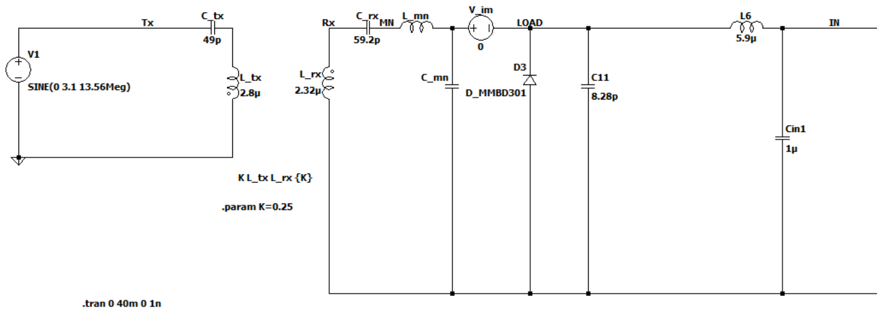

Figure 3.21. SPICE circuit example with general matching network

The input impedance of the matching network (Z_{MN}) and the output impedance of the matching network (Z_{LOAD}) were analytically computed as follows:

$$Z_{\text{MN}} = \frac{\mathbf{V}_{\text{MN}}}{\mathbf{I}_{\text{C\_rx}}} = \frac{A_{V_{\text{MN}}}}{A_{I_{\text{C\_rx}}}} \cdot e^{j\left(\theta_{V_{\text{MN}}} - \theta_{I_{\text{C\_rx}}}\right)} \tag{3.33}$$

$$Z_{\text{LOAD}} = \frac{\mathbf{V}_{\text{LOAD}}}{\mathbf{I}_{\text{V\_im}}} = \frac{A_{V_{\text{LOAD}}}}{A_{I_{\text{V\_im}}}} \cdot e^{j\left(\theta_{V_{\text{LOAD}}} - \theta_{I_{\text{V\_im}}}\right)} \tag{3.34}$$

The input impedance of the rectifier, defined as Z_{LOAD}, was fed into the Matching Network Designer app of MATLAB RF Toolbox to calculate the nominal values of the matching components, L and C. The network was designed to match the load impedance to the target optimal input impedance, defined as $Z_{\text{MN,opt}} = 48.6\,\Omega$. This value is very close to the standard $50\,\Omega$ source impedance, generally used for impedance matching [6].
The idealized L and C values obtained from MATLAB were implemented into the LTspice schematic. An iterative tuning procedure was then performed on the passive components until the simulated input impedance Z_{MN} converged as closely as possible to the target value $Z_{\text{MN,opt}}$.

Chapter 4

LTSpice Simulations

4.1 LTSpice schematic design choices

The complete system was simulated in LTspice in order to evaluate the power flow from the transmitter to the final regulated loads. The simulated architecture includes a sinusoidal voltage source, the transmitting coil, the receiving coil, the resonant compensation capacitors, the matching network, the rectifier stage, and the DC/DC conversion stages, as designed in Chapter 3.

The two coils were modeled as coupled inductors, with self-inductances L_{Tx} and L_{Rx}, series resistances R_{Tx} and R_{Rx}, and magnetic coupling coefficient k.

The transmitter was simulated as an ideal sinusoidal voltage source operating at the ISM frequency $f = 13.56MHz$, set at the minimum V_P value to ensure the correct voltage to the load.

Transient simulations were performed until steady-state conditions were reached. All electrical quantities were then evaluated over the final portion of the simulation window in order to avoid transient effects and obtain stable average values.

For both NerveRepack and Rewire circuits, LTSpice simulations were conducted under four different power conditions, obtained by varying the load resistance. For each power level, three resistance values were used to represent the range of possible loads, as discussed in 3.1.1.

NerveRepack was simulated at 16 mW, 30 mW, 50 mW, and 100 mW. The matching network was designed for two reference conditions: 30 mW and 100 mW (maximum operation).

Rewire was simulated at 24 mW, 30 mW, 50 mW, and 100 mW. The matching network was designed for two reference conditions: 50 mW and 100 mW (maximum operation).

For both circuits, the matching inductance values across the two design points were similar, while the capacitance varied. The matching network parameters for NerveRepack are summarized in Table 4.1, and those for Rewire in Table 4.2.

Power Level	Inductance	Capacitance
30 mW	1.40 μH	90.37 pF
100 mW	1.46 μH	69.77 pF

Table 4.1. Matching network parameters - NerveRepack

Power Level	Inductance	Capacitance
50 mW	1.87 μH	66.03 pF
100 mW	1.76 μH	71.14 pF

Table 4.2. Matching network parameters - Rewire

The small variation in inductance between the two operating points suggested that a single inductor value can cover both conditions, with only the capacitance requiring adjustment. This is the motivation for adopting a trimmer capacitor, as it will be discussed in 5.

4.1.1 Matching Network Refinement Using Real Inductor Models

To determine the most suitable matching network configuration, different combinations of commercially available inductor values were simulated. This step was necessary because the ideal inductance values obtained from the matching network design had to be replaced with real components available on the market.
Coilcraft 1812CS and 1206CS wirewound ceramic chip inductors were selected for the implementation. These series were chosen because they provide high quality factor values and good current-handling capability compared to non-wirewound inductors with similar package dimensions [69] [70]. The use of inductors with an high Q is particularly important at 13.56 MHz, since lower series resistance reduces conduction losses and improves the overall efficiency of the matching network.
When the required inductance value was not directly available as a single component, series of standard inductors were considered in order to approximate the target value while keeping the equivalent series resistance as low as possible.

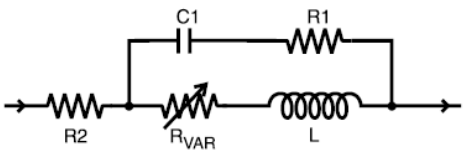

Figure 4.1. Equivalent lumped element model schematic. [71]

The value of the frequency-dependent variable resistor R_{VAR}, associated with the skin effect, is calculated as:[71]

$$R_{\mathrm{VAR}} = k\sqrt{f} \tag{4.1}$$

where:

- k is a coefficient provided for each component value in the accompanying table;
- f is the operating frequency expressed in Hz.

Values	V_{in}	η_{link} [%]	η_{LCtank} [%]	η_{MN} [%]	η_{ret} [%]	η_{DC1} [%]	η_{DC2} [%]	η_{tot} [%]
$L_{\mathrm{MN}} = 1.5\,\mu\mathrm{H}$ $L_{\mathrm{ret}} = 5.6\,\mu\mathrm{H}$	3.88	78.10	99.82	90.31	84.14	42.95	89.44	28.77
$L_{\mathrm{MN}} = 1.5\,\mu\mathrm{H} + 183\,\mathrm{nH}$ $L_{\mathrm{ret}} = 5.6\,\mu\mathrm{H} + 183\,\mathrm{nH}$	3.80	77.92	99.92	90.36	83.62	49.83	89.36	28.92
$L_{\mathrm{MN}} = 1.5\,\mu\mathrm{H} + 183\,\mathrm{nH}$ $L_{\mathrm{ret}} = 5.6\,\mu\mathrm{H}$	3.77	78.86	99.90	88.57	83.51	50.09	89.54	28.80
$L_{\mathrm{MN}} = 1.5\,\mu\mathrm{H}$ $L_{\mathrm{ret}} = 5.6\,\mu\mathrm{H} + 183\,\mathrm{nH}$	3.76	77.92	99.92	90.36	83.62	49.83	89.29	28.92
$L_{\mathrm{MN}} = 1.2\,\mu\mathrm{H}$ $L_{\mathrm{ret}} = 5.6\,\mu\mathrm{H} + 183\,\mathrm{nH}$	3.80	78.63	99.97	91.72	83.49	50.17	89.40	29.80
$L_{\mathrm{MN}} = 1.2\,\mu\mathrm{H}$ $L_{\mathrm{ret}} = 5.6\,\mu\mathrm{H}$	3.79	78.75	99.88	91.69	83.89	49.90	89.46	29.79

Table 4.3. Efficiency evaluation comparison for different matching network configurations for NerveRepack

Given comparable efficiency showed in Table 4.3, the topology requiring fewer inductors with lower inductance values was selected. This choice offered several advantages, including reduced thermal losses, lower parasitic magnetic coupling effects, and a smaller PCB footprint.
In LTspice simulations, constraints on the key voltage values were identified:

- input voltage of the LTC3129-1 above 2.4 V and below 15V
- diode voltage below 30 V

4.1.2 Efficiency evaluation

Figure 4.2 shows the general RF circuit. Components are the same in both circuits, only their values in the matching network change.

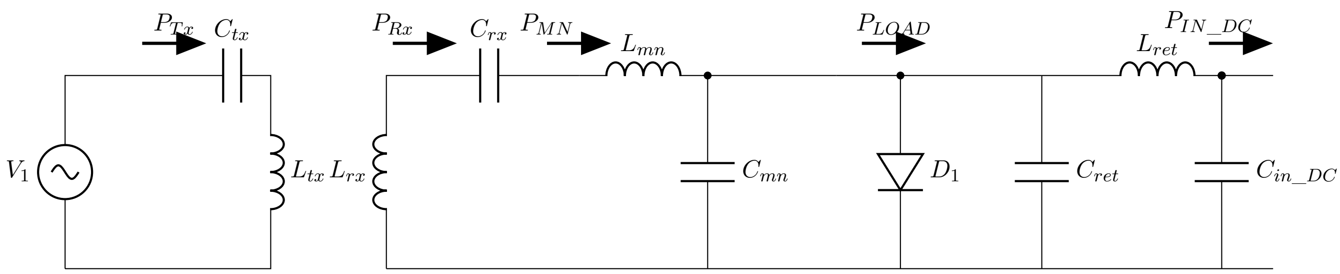

Figure 4.2. Power of interest in the LTSpice schematic

Figures 4.3 and 4.4 show respectively the DC/DC converters stages for NerveRepack and Rewire, with output voltages indications.

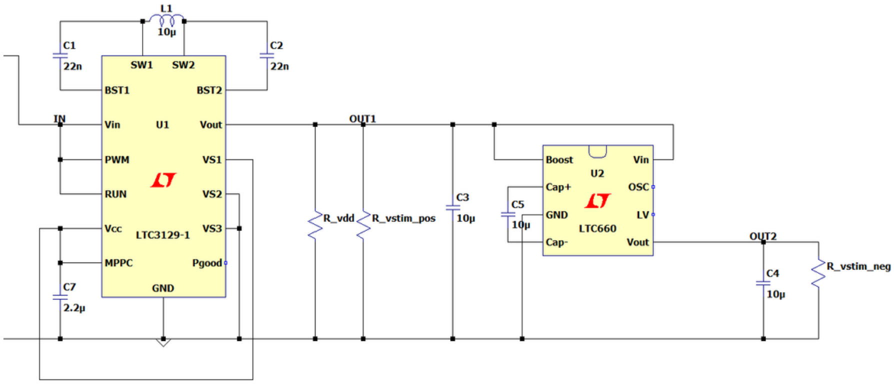

Figure 4.3. NerveRepack DC/DC converters stage

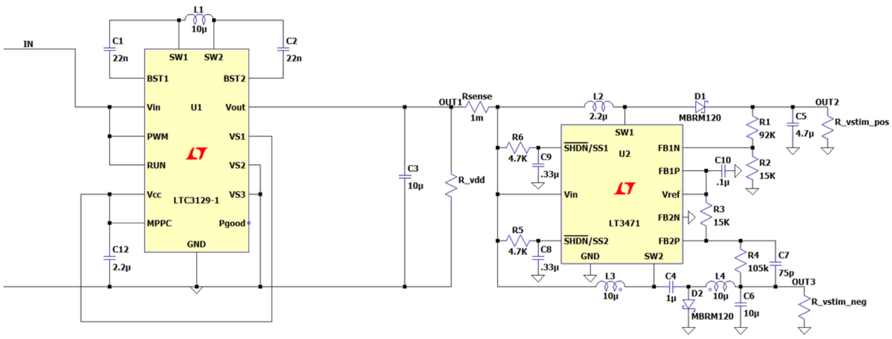

Figure 4.4. Rewire DC/DC converters stage

As illustrated in Figure 4.2 the measured power values were:

- P_{Tx}: average power at the transmitter side:

$$P_{\text{Tx}} = \langle V(\text{Tx}) \cdot I(V_1) \rangle \tag{4.2}$$

- P_{Rx}: average power at the receiving coil:

$$P_{\text{Rx}} = \langle V(\text{Rx}) \cdot I(L_{\text{rx}}) \rangle \tag{4.3}$$

- P_{LCtank}: average power at the resonant tank output, corresponding to the matching network input:

$$P_{\text{LCtank}} = \langle V(\text{MN}) \cdot I(L_{\text{rx}}) \rangle \tag{4.4}$$

- P_{MN}: average power at the matching network output, corresponding to the rectifier input:

$$P_{\mathrm{MN}} = \langle V(\mathrm{load}) \cdot I(V_{\mathrm{im}}) \rangle \tag{4.5}$$

- $P_{\mathrm{IN,DC1}}$: average power at the input of the LTC3129-1 DC/DC converter:

$$P_{\mathrm{IN,DC1}} = \langle V(\mathrm{IN}) \cdot I_x(U_1 : \mathrm{Vin}) \rangle \tag{4.6}$$

To evaluate the efficiency, the average power of each block was computed as follow:

$$P_{\mathrm{avg}} = \frac{1}{t_2 - t_1} \int_{t_1}^{t_2} v(t) i(t) \, dt \tag{4.7}$$

The link efficiency was defined as the ratio between the power received by the secondary coil and the power delivered by the transmitter:

$$\eta_{\mathrm{link}} = \frac{P_{Rx}}{P_{Tx}} \tag{4.8}$$

Similarly, the efficiencies of the matching network, rectifier stage, and DC/DC converters were computed by comparing the output and input powers of each block:

$$\eta_{\mathrm{LCtank}} = \frac{P_{\mathrm{MN}}}{P_{Rx}} \tag{4.9}$$

$$\eta_{\mathrm{MN}} = \frac{P_{\mathrm{LOAD}}}{P_{\mathrm{MN}}} \tag{4.10}$$

$$\eta_{\mathrm{rect}} = \frac{P_{\mathrm{IN,DC}}}{P_{\mathrm{LOAD}}} \tag{4.11}$$

η_{DC} calculations changed for NerveRepack and Rewire.
For NerveRepack:

$$\eta_{\mathrm{DC1}} = \frac{P_{\mathrm{out1}} + P_{\mathrm{out2}}}{P_{\mathrm{in,U1}}} \tag{4.12}$$

$$\eta_{\mathrm{DC2}} = \frac{P_{\mathrm{out3}}}{P_{\mathrm{in,U2}}} \tag{4.13}$$

For Rewire:

$$\eta_{\mathrm{DC1}} = \frac{P_{\mathrm{out1}}}{P_{\mathrm{in,U1}}} \tag{4.14}$$

$$\eta_{\mathrm{DC2}} = \frac{P_{\mathrm{out2}} + P_{\mathrm{out3}}}{P_{\mathrm{in,U2}}} \tag{4.15}$$

Finally, the overall system efficiency was calculated as the ratio between the total power delivered to the regulated loads and the power generated by the transmitter source.

$$\eta_{\mathrm{tot}} = \frac{P_{\mathrm{out,tot}}}{P_{Tx}} \tag{4.16}$$

where $P_{\text{out,tot}}$ is the total output power delivered to the regulated loads, defined as

$$P_{\text{out,tot}} = P_{\text{out1}} + P_{\text{out2}} + P_{\text{out3}}. \tag{4.17}$$

LOAD	**MN LOAD**	$\eta_{\textbf{link}}$ [%]	$\eta_{\textbf{lctank}}$ [%]	$\eta_{\textbf{mn}}$ [%]	$\eta_{\textbf{ret}}$ [%]	$\eta_{\textbf{dc1}}$ [%]	$\eta_{\textbf{dc2}}$ [%]	$\eta_{\textbf{tot}}$ [%]
16 mW	30	77.93	99.91	99.57	87.85	50.46	89.51	34.09
	100	78.25	99.97	99.64	89.59	45.57	89.48	31.46
30 mW	30	77.57	99.77	99.47	88.33	63.28	93.98	42.93
	100	78.70	99.94	99.60	90.79	57.06	93.95	40.33
50 mW	30	77.79	99.81	99.52	90.93	67.50	96.03	47.38
	100	78.20	99.98	99.64	92.61	62.67	96.04	45.03
100 mW	30	76.87	99.90	99.46	91.56	77.52	97.24	54.16
	100	79.39	99.55	99.53	92.87	74.50	97.23	54.67

Table 4.4. Block efficiencies of the NerveRepack circuit.

LOAD	**MN LOAD**	$\eta_{\textbf{link}}$ [%]	$\eta_{\textbf{lctank}}$ [%]	$\eta_{\textbf{mn}}$ [%]	$\eta_{\textbf{ret}}$ [%]	$\eta_{\textbf{dc1}}$ [%]	$\eta_{\textbf{dc2}}$ [%]	$\eta_{\textbf{tot}}$ [%]
24 mW	50	79.58	99.99	99.92	91.21	58.67	50.53	27.76
	100	78.66	99.86	99.58	90.30	62.80	50.54	29.02
30 mW	50	79.36	99.96	99.61	92.06	61.81	54.10	30.78
	100	78.55	99.82	99.57	90.82	65.42	54.13	31.85
50 mW	50	79.06	99.61	99.92	92.66	68.31	62.92	37.77
	100	78.64	99.87	99.59	92.02	69.90	62.92	38.19
100 mW	50	78.42	99.98	99.59	93.51	75.74	72.59	45.95
	100	78.42	99.87	99.58	93.40	75.97	72.58	46.04

Table 4.5. Block efficiencies of the Rewire circuit.

Tables 4.4 and 4.5 report the efficiency of each functional block of the two receiver architectures for different load conditions and matching network configurations.
For both the NerveRepack and Rewire receivers, the resonant tank exhibits the highest efficiency, remaining above 99.8% in all operating conditions. Similarly, the matching network introduces only limited losses, with efficiencies close to 99.5%, demonstrating that the passive RF stages were properly designed and tuned.
The inductive link efficiency remains nearly constant, between approximately 77% and 80%, showing a slight dependence on the load condition. This behavior is expected because the coupling coefficient and the coil geometry remain unchanged throughout the measurements.
The Class-E rectifier also achieves high efficiencies, ranging from approximately 88% to 94%. A slight improvement can be observed as the load power increases, confirming that the rectifier operates more efficiently at higher transferred power levels.

The largest efficiency variations are observed in the DC/DC conversion stages. For the NerveRepack receiver, the efficiency of the LTC3129-1 increases from approximately 45% at 16 mW to more than 77% at 100 mW, while the LTC660 efficiency increases from about 89% to over 97%. Similarly, in the Rewire receiver, both the LTC3129-1 and the LT3471 exhibit a significant efficiency improvement as the output power increases. These results indicate that the DC/DC converters represent the dominant source of losses, particularly under low-power operating conditions, where switching and quiescent losses become more significant. This behavior is consistent with the efficiency curves reported in the LTC3129-1 datasheet, shown in Figure 4.5. As the output current decreases, the converter efficiency drops significantly, especially in PWM operation. Therefore, the measured efficiency trend is mainly limited by the operating range of the selected DC/DC converters rather than by the inductive link alone.

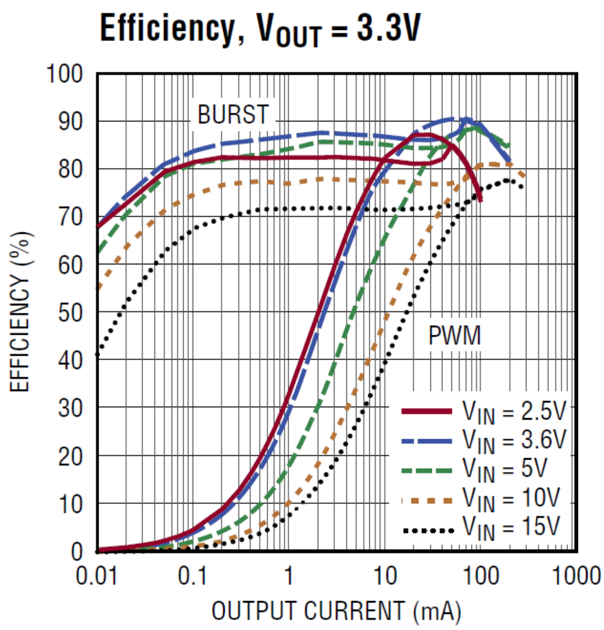

Figure 4.5. Efficiency of the LTC3129-1 converter for $V_{\mathrm{OUT}} = 3.3\,\mathrm{V}$ as a function of the output current. [56]

Overall, the results confirm that the passive RF stages are already highly efficient, whereas further improvements in the overall receiver efficiency should mainly focus on the DC/DC conversion stage.

4.1.3 Coupling coefficient variation

The influence of the coupling coefficient k on the receiver performance was also investigated. The transmitter voltage was initially kept constant at the minimum voltage required to obtain the desired output, while the coupling coefficient was varied from 0.1 to 0.8.

k	V_s [V]	V_{out1} [V]	V_{out2} [V]	V_{in} [V]	η_{link} [%]	η_{ret} [%]	η_{dc1} [%]	η_{dc2} [%]	η_{tot} [%]
0.1	2.7	3.30	-3.30	10.58	48.39	95.19	26.06	89.36	11.80
0.2	2.7	3.30	-3.30	5.42	74.19	91.19	40.79	89.50	26.97
0.3	3.2	3.30	-3.30	3.80	79.98	88.09	49.87	89.47	34.55
0.4	4.2	3.30	-3.30	3.86	82.07	88.25	49.38	89.51	35.17
0.5	5.0	3.30	-3.30	3.50	83.39	87.20	51.93	89.56	37.16
0.6	6.0	3.30	-3.30	3.55	83.86	87.33	51.79	89.54	37.33
0.7	6.9	3.30	-3.30	3.45	83.97	87.08	52.19	89.41	37.57
0.8	7.9	3.30	-3.30	3.35	84.30	86.42	52.60	90.10	37.77

Table 4.6. Effect of the coupling coefficient on the performance of the NerveRepack receiver with a variable transmitter voltage.

k	V_s [V]	V_{out1} [V]	V_{out2} [V]	V_{out3} [V]	V_{in} [V]	η_{link} [%]	η_{ret} [%]	η_{dc1} [%]	η_{dc2} [%]	η_{tot} [%]
0.1	3.1	3.30	7.13	-7.00	13.60	43.90	63.49	16.35	48.72	6.87
0.2	3.1	3.30	7.13	-7.00	9.25	72.14	94.48	20.44	48.73	21.03
0.3	3.7	3.30	7.13	-7.00	4.44	84.76	84.27	27.44	48.49	29.35
0.4	4.5	3.30	7.13	-7.00	4.44	84.76	84.27	27.44	48.49	29.35
0.5	5.4	3.30	7.13	-7.00	3.61	85.10	76.70	31.01	55.43	28.21
0.6	6.2	3.30	7.12	-7.00	3.85	85.40	78.20	30.50	55.80	29.10
0.7	7.0	3.30	7.12	-7.00	4.05	85.80	80.10	29.70	56.10	30.20
0.8	7.8	3.30	7.13	-7.00	4.25	86.10	82.00	28.90	56.40	31.40

Table 4.7. Effect of the coupling coefficient on the performance of the ±7 V receiver with a variable transmitter voltage.

As reported in Tables 4.6 and 4.7, increasing the coupling coefficient improves the efficiency of the inductive link, which rises from 48.39% at $k = 0.1$ to more than 85% at $k = 0.7$ in NerveRepack and from 43.90% to 86.10% in Rewire. However, the receiver is able to regulate the desired output voltages only up to $k = 0.2$. For higher coupling coefficients, the voltage delivered to the DC/DC converters becomes insufficient, resulting in the loss of voltage output regulation.
This behavior can be explained by the variation of the reflected impedance with the coupling coefficient. As the coupling coefficient increases, the input voltage supplied to the DC/DC converters decreases. Consequently, the converters are no longer able to operate within their regulation range, leading to a loss of output voltage regulation.
To restore the nominal output voltages at higher coupling coefficients, the transmitter voltage must be increased. In particular, the transmitter voltage had to be increased from 2.7 V to 3.2 V for $k = 0.3$ and up to 7.9 V for $k = 0.8$ for NerveRepack and from a minimum of 3.1 V to a maximum of 7.8 V in Rewire. Under these conditions, the receivers successfully reached the nominal output voltages, while the overall efficiency increased to 37.77% in NerveRepack and to 31.40% in Rewire.

Chapter 5

Printed Circuit Board Design

The printed circuit boards (PCBs) were designed in Altium Designer, a PCB software design which allows schematic and layout editors. Firstly, components were chosen following the Spice simulation requirements, and then eventually imported. Secondly, PCB schematics and layout were designed.

5.1 Schematic

Figures 5.1 and 5.2 show the electrical schematic of the receiver boards for NerveRepack and Rewire, respectively. Both boards share the same general architectures, which consist of four main blocks: the receiving circuit, the matching network, the Class-E rectifier and the DC/DC converters stage. The main differences between the two schematics are related to the values of the inductance and capacitance used in the matching network and to the DC/DC conversion stage. In the NerveRepack receiver, the -3.3 V supply rail is generated using the LTC660, whereas in the Rewire receiver the LT3471 is used to generate ± 7 V.

Two JZ500 trimmer capacitors, with an adjustable range from 8 pF to 50 pF, were placed in parallel with the fixed capacitances of the receiving resonant tank and matching network. This allowed the effective capacitance to be tuned around the values obtained from SPICE simulations.

This tuning is required because component tolerances, parasitic capacitances, coil inductance variations, and changes in coil positioning can shift the resonance frequency and alter the impedance matching condition. By adjusting the trimmers, the receiver can be brought back close to resonance at 13.56 MHz and the impedance seen by the inductive link can be optimized. This improves power transfer to the rectifier, reduces reflected power, and allows the required output voltages to be obtained with lower transmitter input power. [72] Several headers were connected to the configuration pins of the DC/DC converters to enable different operating modes during testing. Additional headers were placed at the converter outputs to allow the connection of external load resistors through a breadboard during the experimental characterization phase.

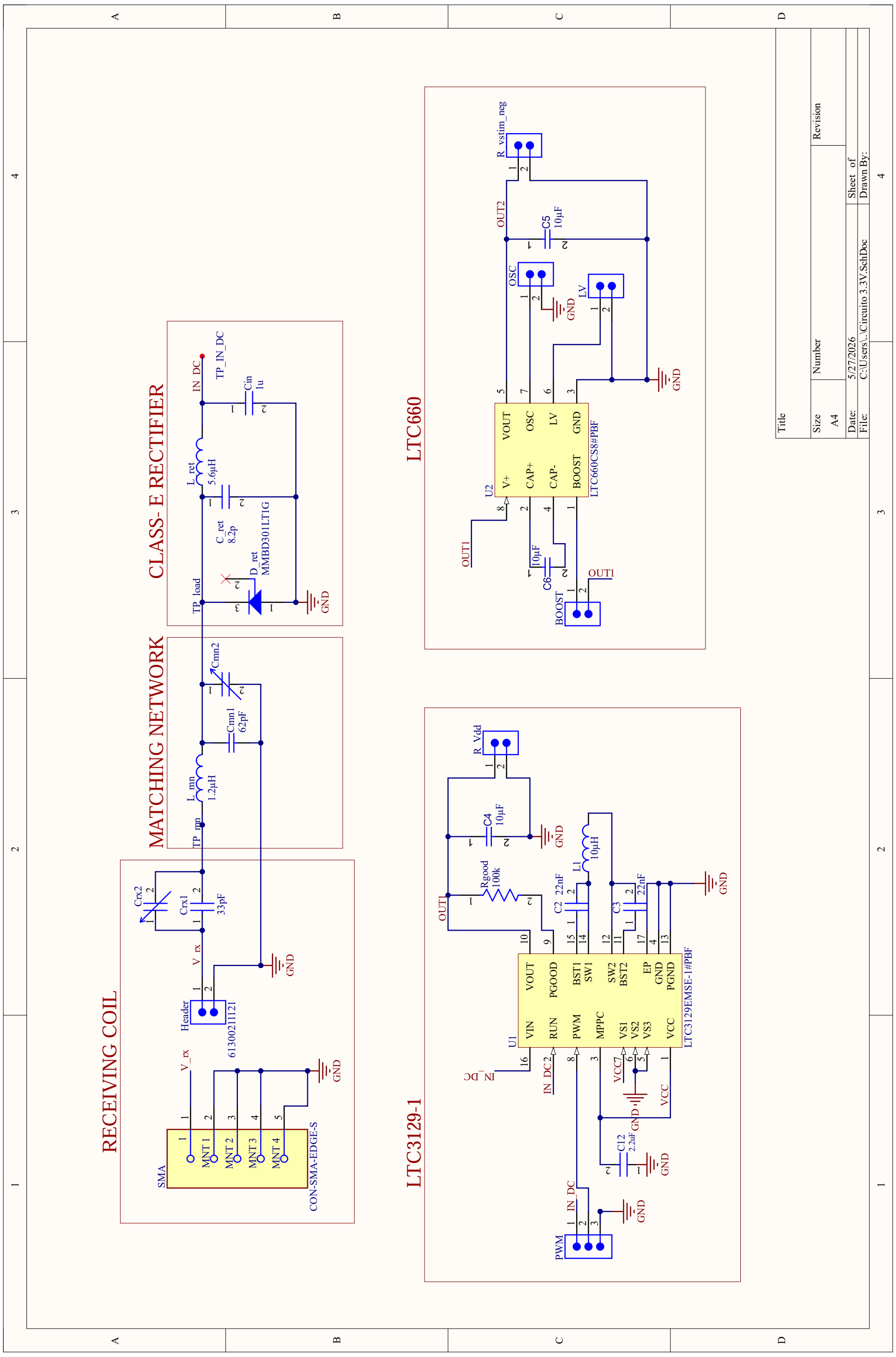

Figure 5.1. Altium schematic for NerveRepack circuit

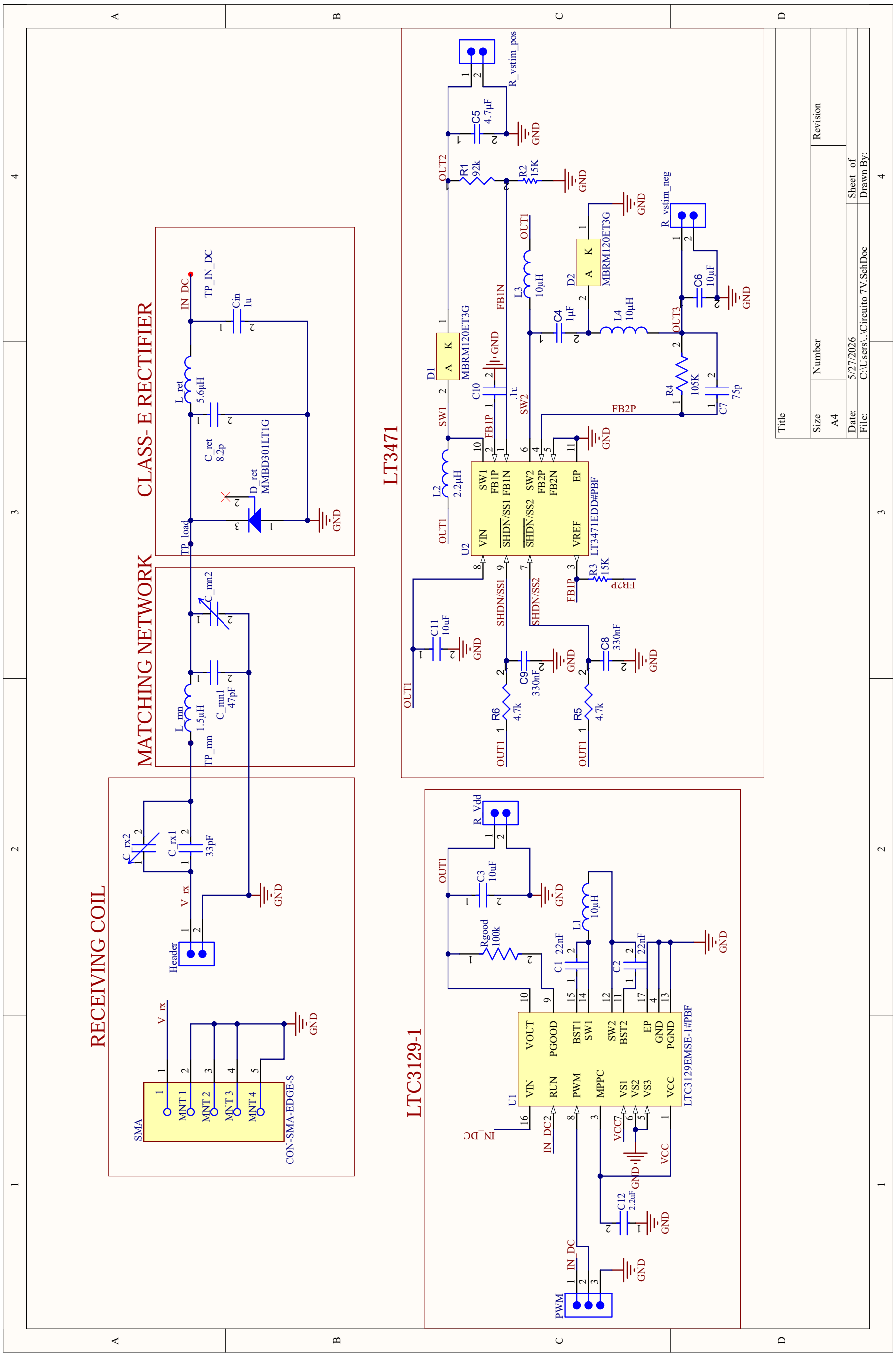

Figure 5.2. Altium schematic for Rewire circuit

5.2 PCB Layout

Figure 5.3 illustrates the layout of the receiver board developed for NerveRepack, with overall dimensions of 56.7 mm x 21.8 mm.
Figure 5.4 illustrates the layout of the receiver board designed for Rewire, which measures 68.9 mm x 30.9 mm.
Since the receiver operates at 13.56 MHz and includes both RF and switching power stages, PCB layout plays a fundamental role in minimizing parasitic effects and ensuring stable operation. Several choices were made when designing the boards:

- The PCB layout follows the signal flow of the receiver architecture, with the matching network, rectifier, and DC/DC conversion stages arranged sequentially from left to right;

- Test points were included at critical nodes of the circuit to facilitate experimental characterization of the individual stages during laboratory measurements;

- The SMA connector was placed as close as possible to the left edge of the PCB, to facilitate the connection with the receiving coil;

- The matching network and rectifier were located close to the SMA connector in order to reduce parasitic effects associated with PCB traces. Furthermore, the power conversion stages were placed in a separate area of the board to limit possible interference between the RF section and the switching converters;

- The RF paths were designed to be as short and direct as possible, using wider traces to reduce resistive losses and improve current handling capability. Since the system operates at 13.56 MHz, the PCB traces cannot be considered ideal interconnections, as they exhibit parasitic resistance, capacitance, and inductance that may affect circuit performance;

- Vias were avoided along the RF signal path to prevent additional parasitic inductance and impedance discontinuities;

- A two-layer PCB structure was adopted for both designs. Large copper polygon pours were implemented on both the top and bottom layers to provide a low-impedance ground reference and improve the overall grounding performance. Additional copper pours were used in the DC/DC converter sections according to the layout recommendations provided in the corresponding datasheets [57, 56, 59];

- The bypass capacitors were placed as close as possible to the power pins of the converters in order to minimize the current loop area and reduce supply voltage noise.

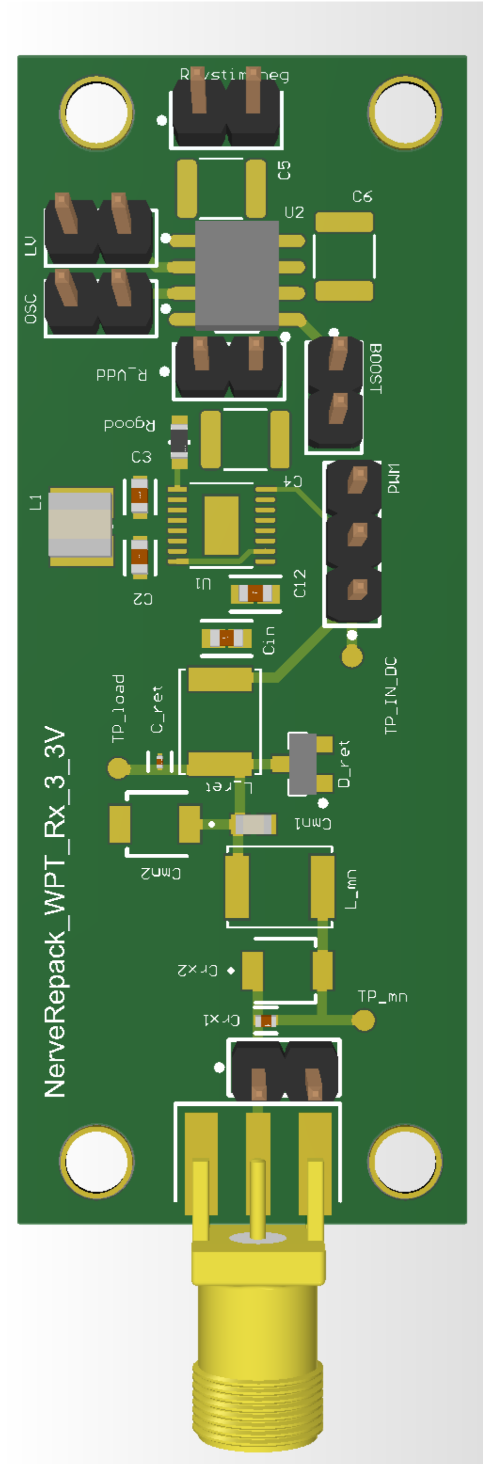

Figure 5.3. 3D view of NerveRepack PCB

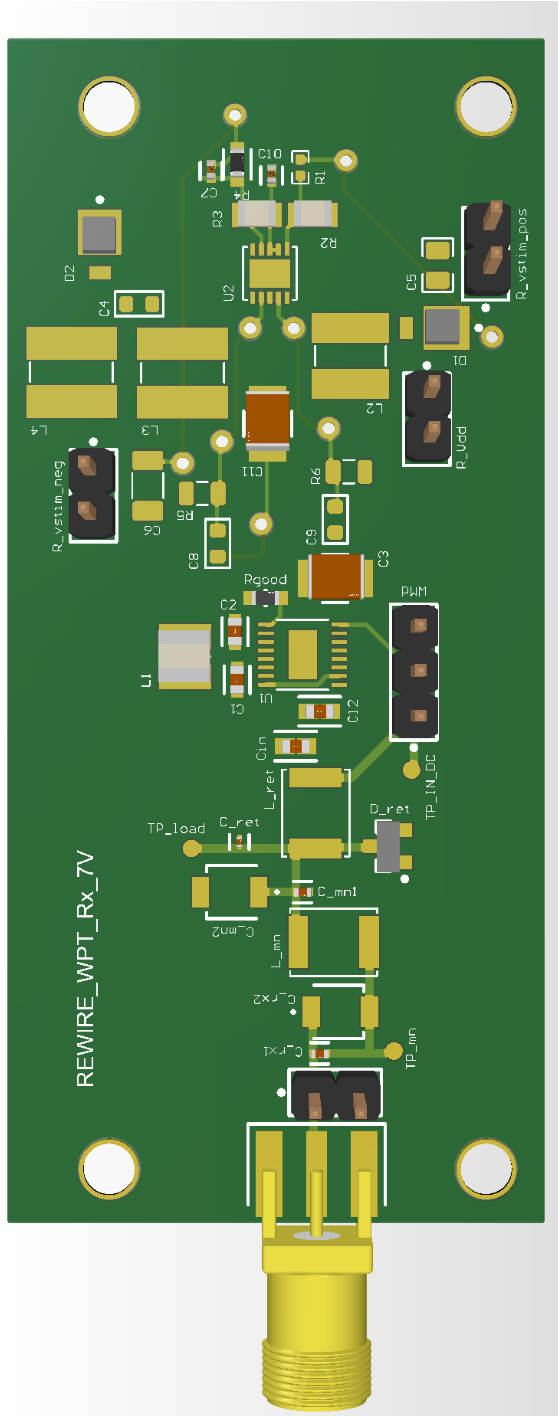

Figure 5.4. 3D view of Rewire PCB

Chapter 6

Tests and Results

The PCB prototypes were tested in the laboratory, to compare the simulation results to those under real conditions. The equipment used to evaluate the performance of the circuits consisted of a DC power supply, a multimeter and an Arduino UNO R4 Wi-fi board. The receiver prototypes were experimentally characterized using a custom 13.56 MHz Class-E wireless power transmitter developed within the research group [73]. Although the transmitter is not the subject of this work, it provides the RF excitation required to evaluate the receiver under realistic operating conditions. The transmitted power can be adjusted by varying the supply voltage through an MP8859 DC/DC converter [65] controlled by an Arduino UNO R4 Wi-Fi board, allowing the transmitter supply voltage to be adjusted in order to achieve the desired regulated output voltage at the load. The transmitter side of the circuit was powered by a DC power supply set to 5 V and limited to 200 mA. Initial measurements were performed with the transmitter and receiver coils aligned at a separation distance of 1 cm, corresponding to a coupling coefficient value of $k = 0.25$, as described in 3.1.1.
Resistive loads were connected to the output pins of the DC/DC converters through a breadboard in order to emulate the different operating load conditions.
The output voltages were regulated by adjusting the trimmer capacitance values, which modify the equivalent capacitance of the receiving resonant tank and matching network. This tuning changes the resonance and impedance matching conditions, controlling the voltage transferred to the rectifier input and therefore the DC voltage available at the output. In this way, the desired output voltages were achieved while minimizing the required transmitter input power. The transmitter input power $P_{\text{in,TX}}$ì, was read directly from the power supply, while the output power delivered to each load was calculated according to:

$$P_{\text{out}} = \frac{V_{\text{out}}^2}{R_{\text{load}}}. \tag{6.1}$$

The total output power was then obtained by summing the power contributions of all loads. Finally, the overall system efficiency was calculated as:

$$\eta_{\text{tot}}[\%] = \frac{P_{\text{out,tot}}}{P_{\text{in,TX}}} \times 100 \tag{6.2}$$

where $P_{\text{out,tot}}$ is the total power delivered to the regulated loads and P_{in} is the power supplied by the transmitter source.

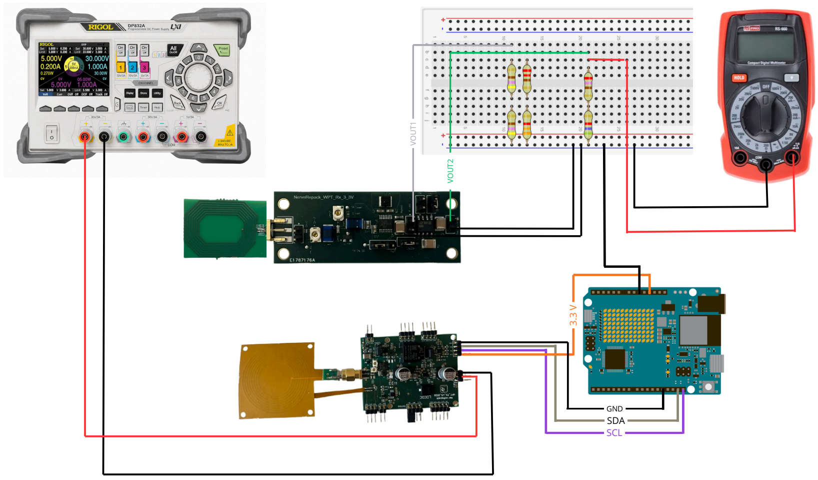

Figure 6.1. Demonstration of measurement setup

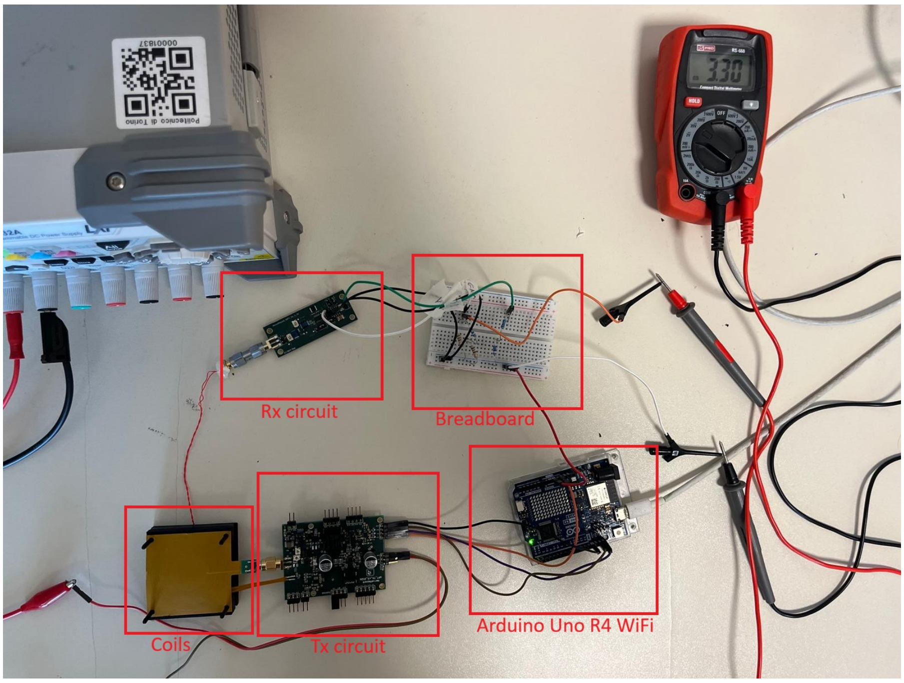

Figure 6.2. Measurement setup for NerveRepack circuit - 3.3 V Output

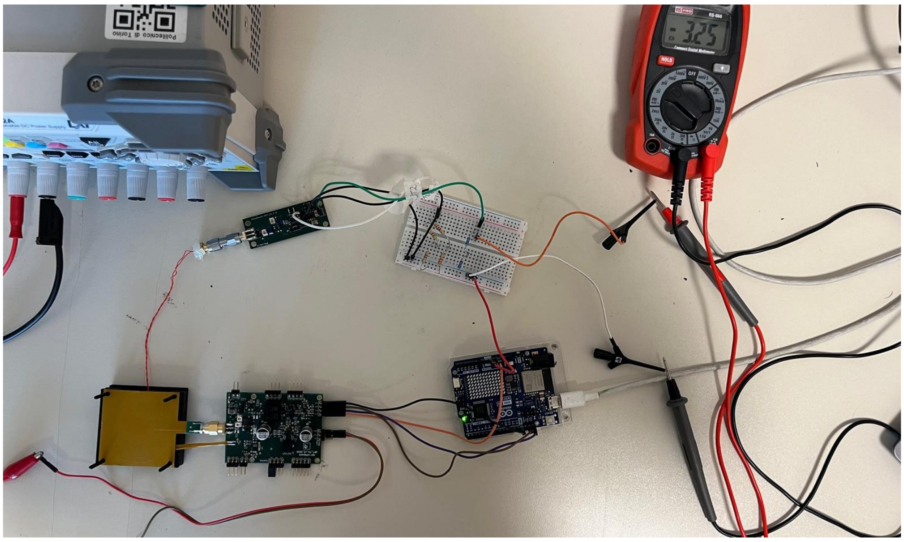

Figure 6.3. Measurement setup for NerveRepack circuit - -3.3 V Output

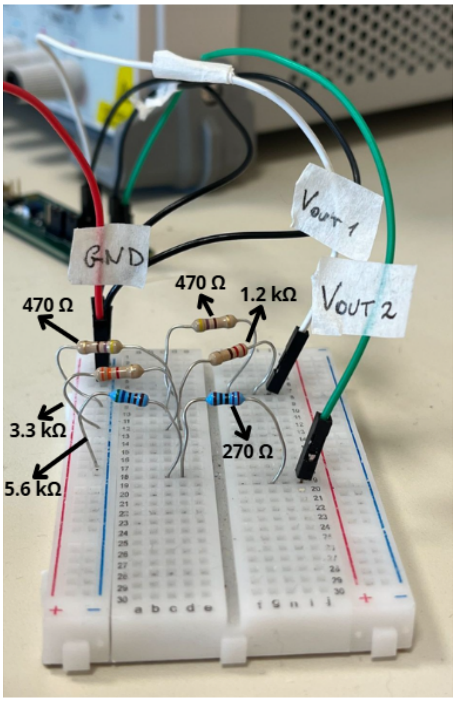

Figure 6.4. 16 mW load resistances disposition

Table 6.1 shows measured performance of the NerveRepack receiver with MP8859 input voltage set to 5 V.

P_{in} [mW]	P_{out} [mW]	η_{tot} [%]
153	16	10.5
190	30	15.8
215	50	23.3
295	100	33.9

Table 6.1. Measured performance of the NerveRepack receiver with MP8859 input voltage set to 5 V.

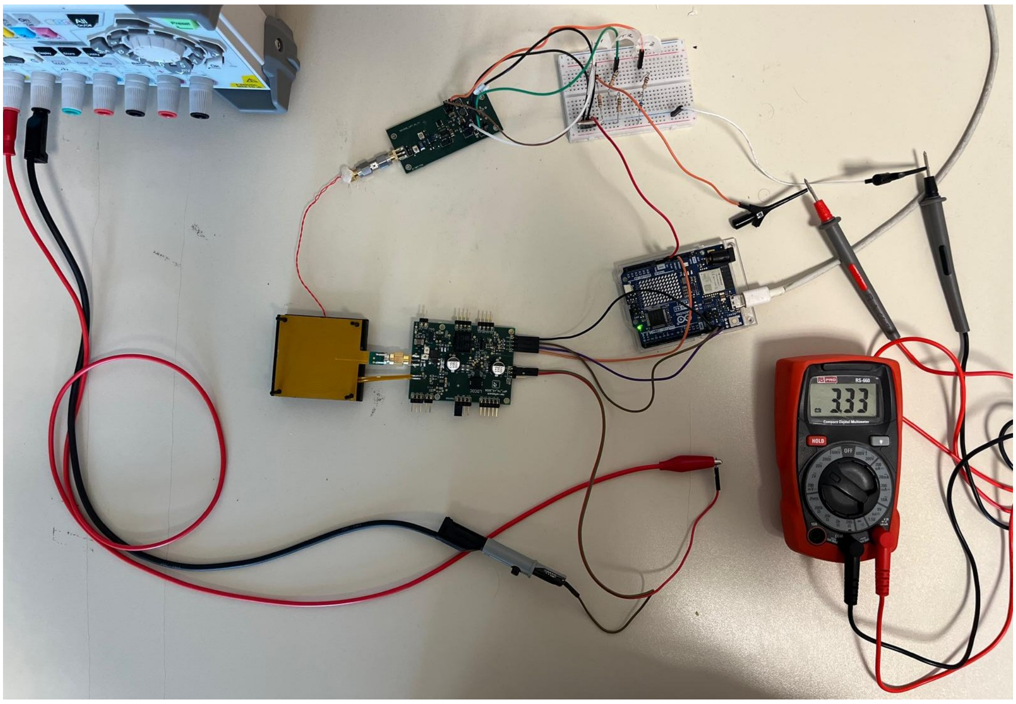

Figure 6.5. Measurement setup for Rewire circuit - 3.3 V Output

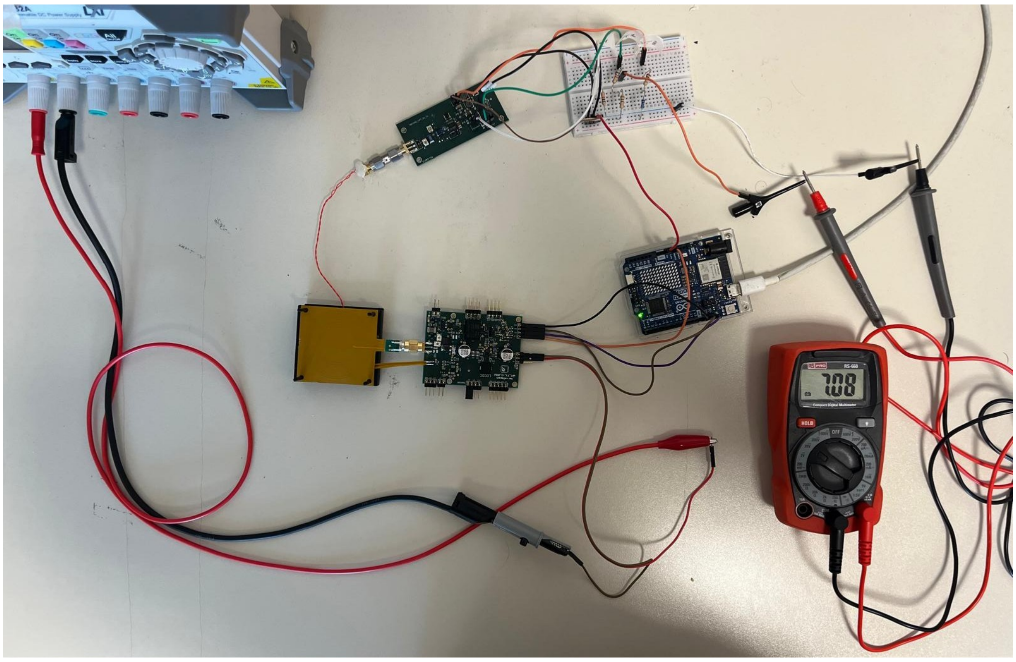

Figure 6.6. Measurement setup for Rewire circuit - 7 V Output

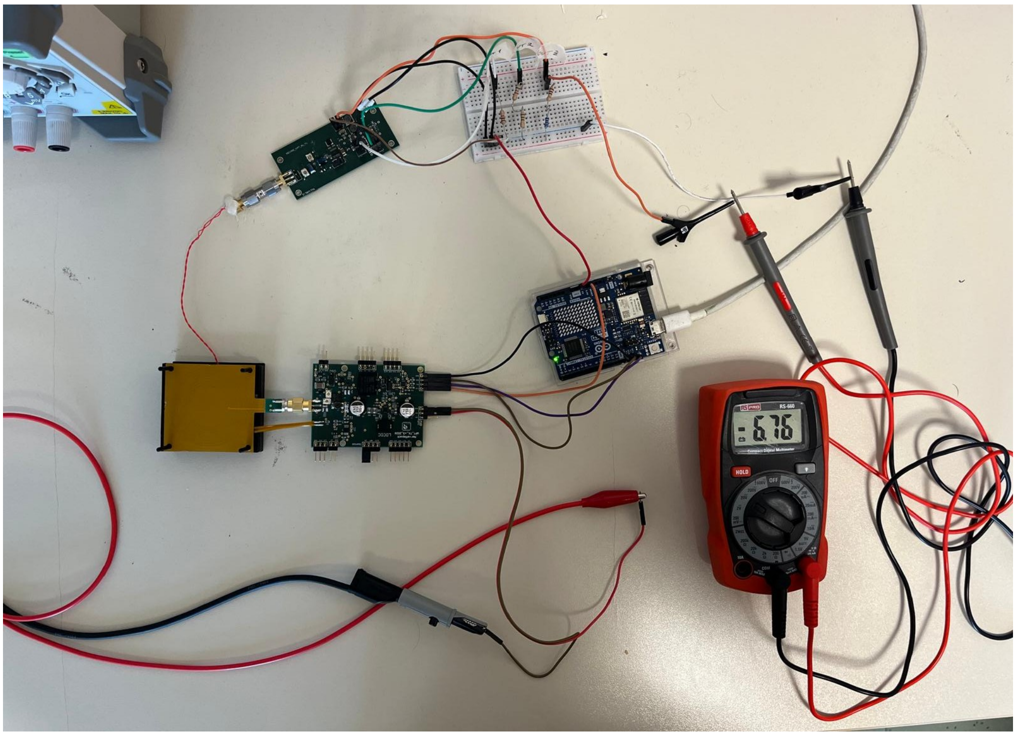

Figure 6.7. Measurement setup for Rewire circuit - -7 V Output

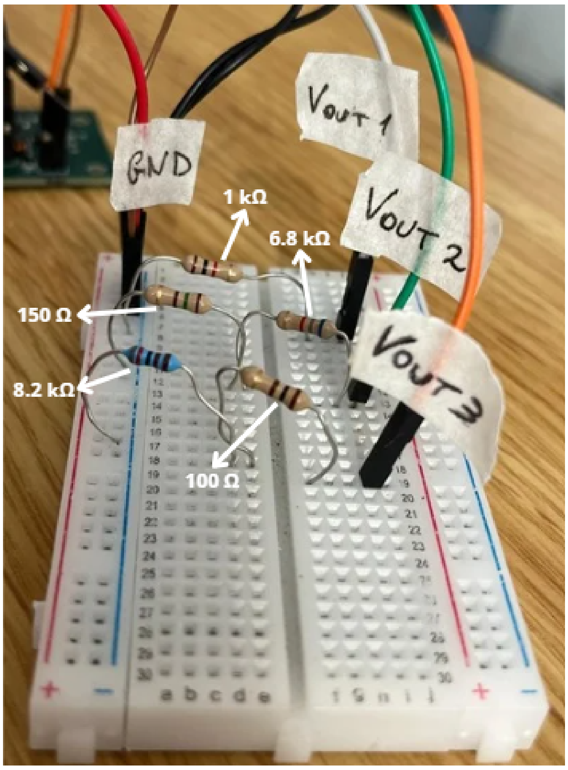

Figure 6.8. 24 mW load resistances disposition

Table 6.2 shows measured performance of the Rewire receiver with MP8859 input voltage set to 10.5 V.

P_{in} [mW]	P_{out} [mW]	η_{tot} [%]
270	24	8.9
305	30	9.8
370	50	13.5
505	100	19.4

Table 6.2. Measured performance of the Rewire receiver with MP8859 input voltage set to 10.5 V.

Figures 6.9 and 6.10 compare the simulated and experimentally measured overall efficiency of the NerveRepack and Rewire receivers under their load conditions.

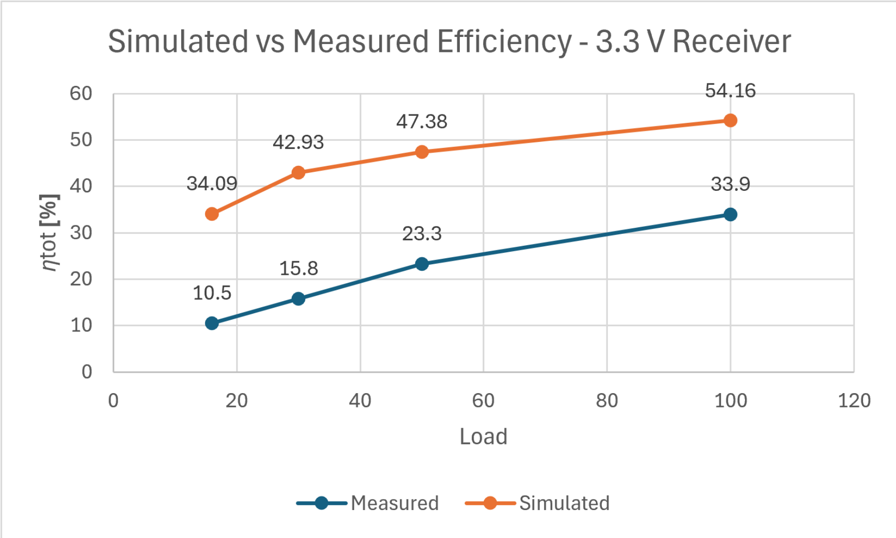

Figure 6.9. Simulated vs Measured Efficiency - NerveRepack Receiver

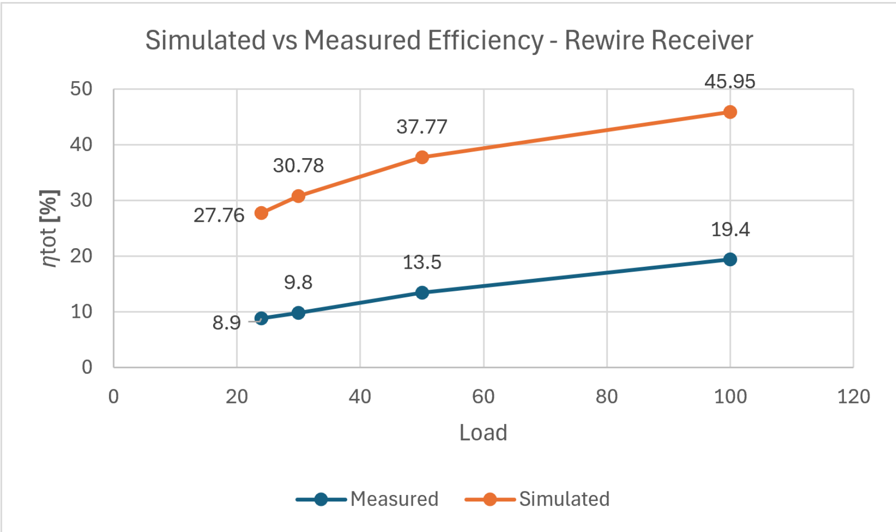

Figure 6.10. Simulated vs Measured Efficiency - Rewire Receiver

Both curves show the same increasing trend with the output power, indicating that the experimental behavior is consistent with the simulated one. In both receiver architectures, the overall efficiency increased with the output power level, reaching a maximum measured value of 33.9% for the NerveRepack receiver and 19.4% for the Rewire receiver at 100 mW output power. The laboratory efficiency results are lower than the simulated ones for all output power levels. This discrepancy is mainly due to the fact that in the LTSpice model, the transmitter was represented by an ideal sinusoidal voltage source, neglecting the losses associated with the transmitter electronics and power supply. The experimental measurements include the complete transmitter chain, including the MP8859 converter and the transmitter circuitry, resulting in a lower overall measured efficiency.

6.0.1 Misalignments Tests

To evaluate the robustness of the wireless power link, additional tests were performed under vertical, lateral and angular coil misalignment conditions. The measurements were carried out under the standard operating power conditions, corresponding to 16 mW for the NerveRepack receiver and 24 mW for the Rewire receiver.

Custom 3D-printed mechanical structures were realized to evaluate vertical, lateral and angular displacements. The position of the Tx coil was adjusted relative to that of the Rx coil.

Vertical Displacement

Vertical misalignments were verified in the standard load conditions (16 mW for NerveRepack and 24 mW for Rewire) considering a distance between coils from 0.6 cm to 1.4 cm in 2 mm steps. Both Rx and TX coils were aligned.

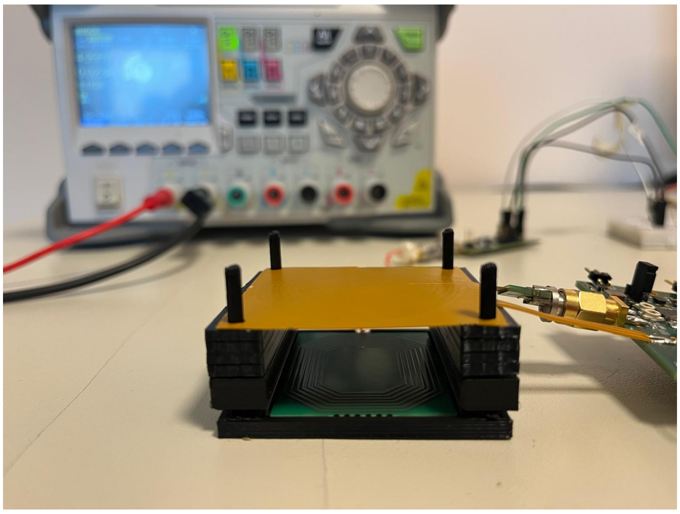

Figure 6.11. Example of 1.4 cm vertical misalignment.

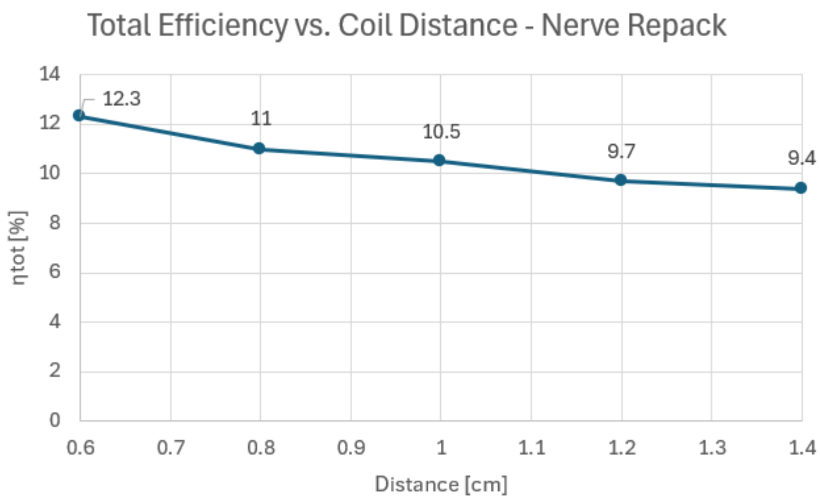

Figure 6.12. Effect of vertical coil misalignment on system efficiency for the NerveRepack receiver at 16 mW output power.

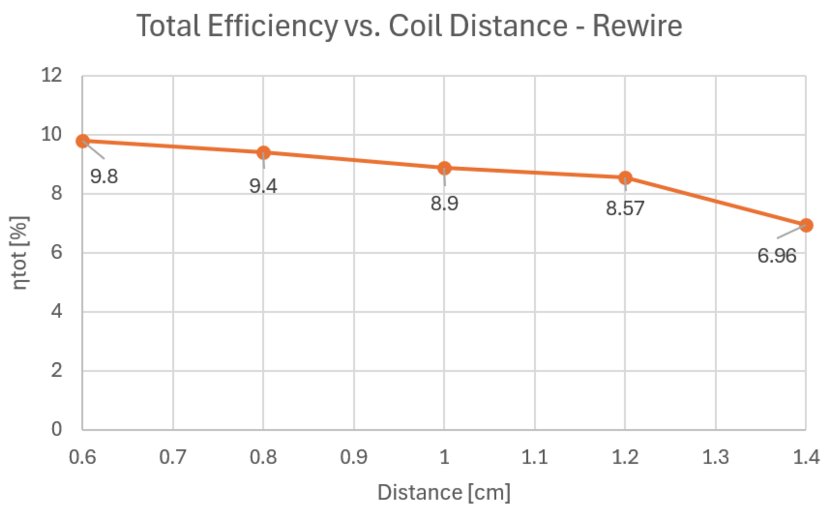

Figure 6.13. Effect of vertical coil misalignment on system efficiency for the Rewire receiver at 24 mW output power.

The results shown in Figures 6.12 and 6.13 show that the overall efficiency decreases as the separation distance between the transmitter and receiver coils increases. This behavior is expected because the mutual inductance and coupling coefficient decrease with increasing coil separation. As a consequence, a larger input power is required to maintain the same regulated output power, resulting in a reduction of the overall system efficiency [74].

Lateral Displacement

Lateral misalignments were evaluated from 0.2 cm to 1.2 cm in 2 mm steps. Both TX and RX coils were aligned at a distance of 10 mm.

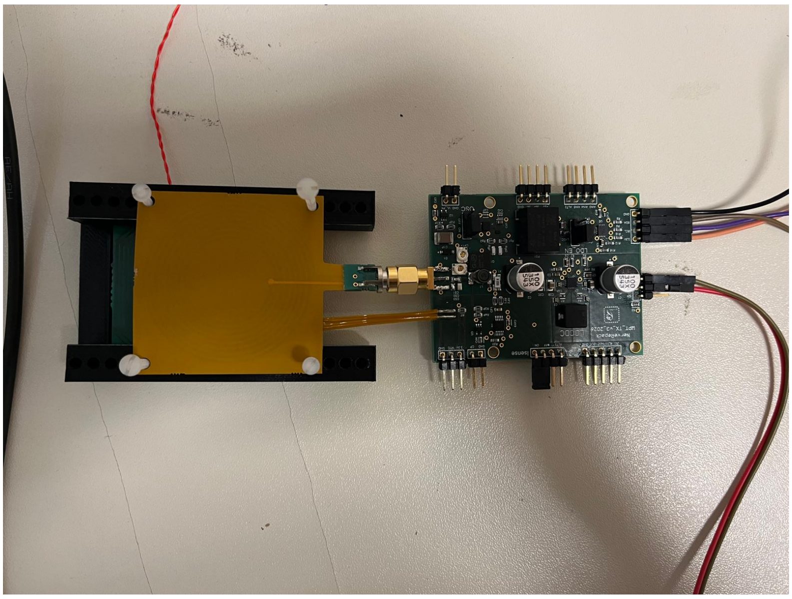

Figure 6.14. Example of 0.8 cm lateral misalignment

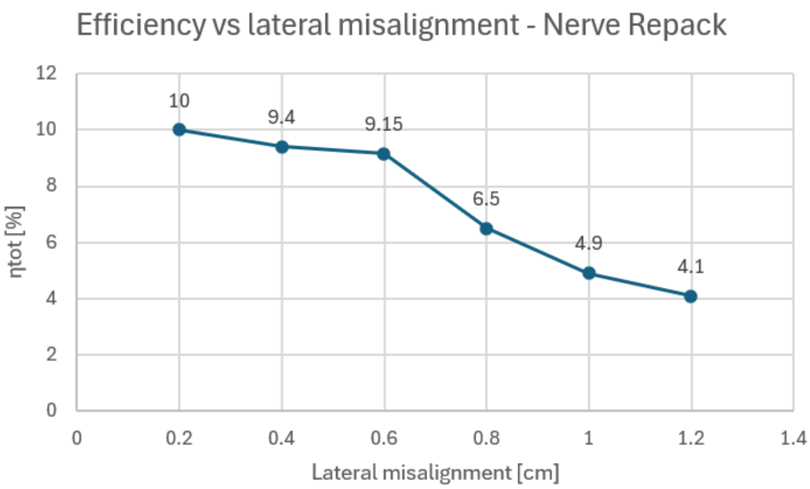

Figure 6.15. Effect of lateral coil misalignment on system efficiency for the NerveRepack receiver at 16 mW output power.

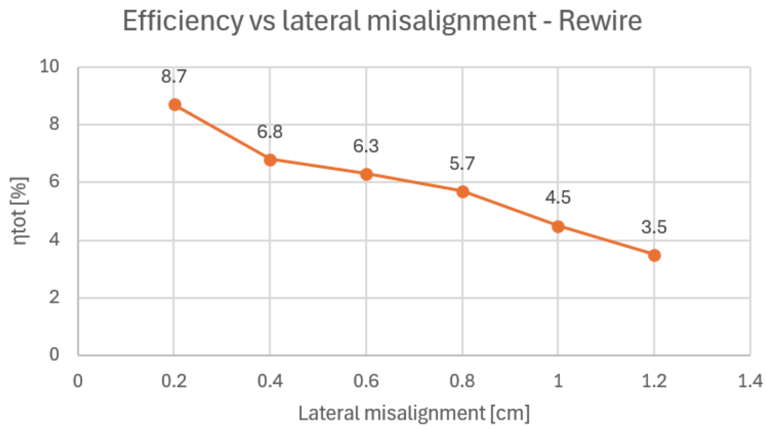

Figure 6.16. Effect of lateral coil misalignment on system efficiency for the Rewire receiver at 24 mW output power.

Lateral misalignment tests showed a progressive degradation of the system performance as the lateral displacement increased. Both receiver architectures maintained stable operation up to a lateral misalignment of 0.6 cm. At 0.8 cm and beyond, the minimum MP8859 input voltage was insufficient to sustain the required output voltages. Consequently, the input voltage was increased to the maximum value allowed by the MP8859.

Angular Displacement

Angular displacements were evaluated from 2° to 14° in 2° steps, with both Tx and Rx coil aligned.

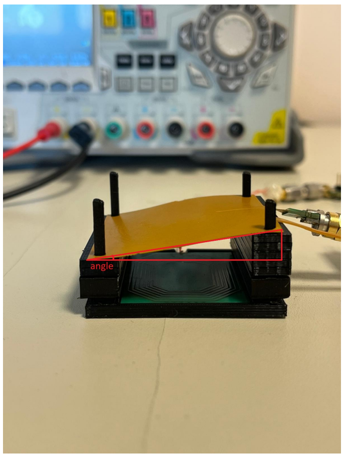

Figure 6.17. Example of angular displacement

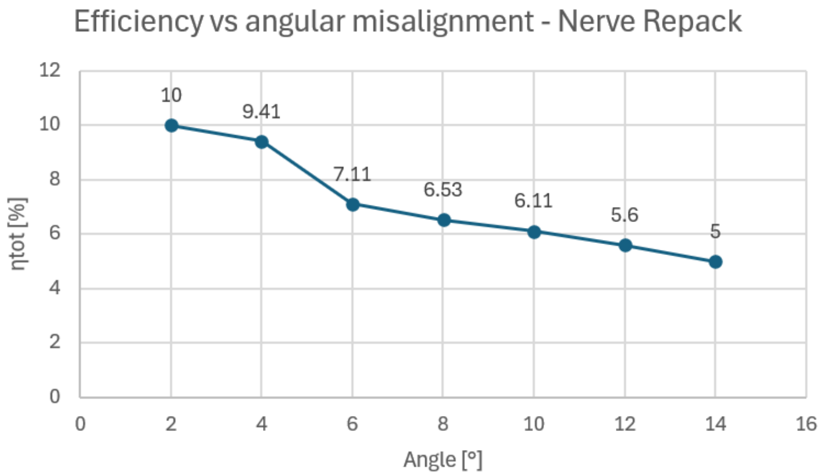

Figure 6.18. Effect of angular misalignment on system efficiency for the NerveRepack receiver at 16 mW output power

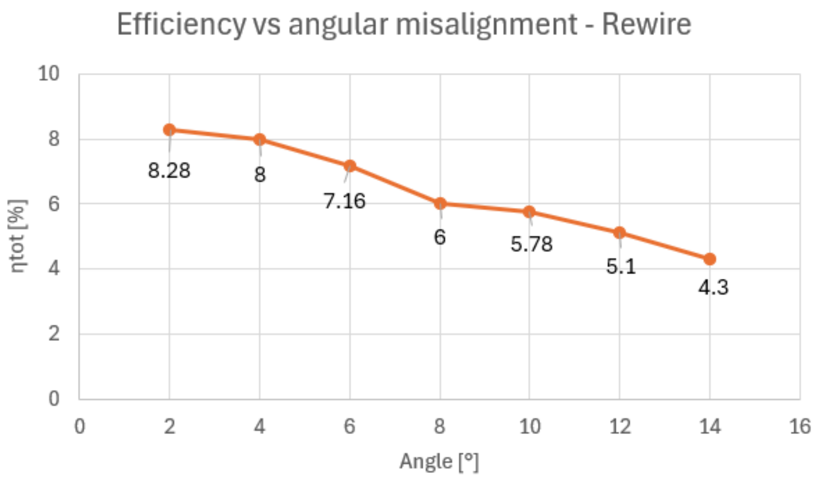

Figure 6.19. Effect of angular misalignment on system efficiency for the Rewire receiver at 24 mW output power.

For angular displacements higher than 10°, the MP8859 input voltage was increased to its maximum value of 15 V in an attempt to maintain the required regulated output voltages.

Overall, the misalignment tests confirmed that the efficiency of the inductive link is strongly affected by the relative positioning of the transmitter (Tx) and receiver (Rx) coils. Vertical displacement produced a progressive reduction in the overall efficiency as the coil separation increased, due to the decrease in mutual inductance and coupling coefficient.

Lateral misalignment had an even more pronounced impact on system performance. As shown in Figures 6.15 and 6.16, both receiver architectures were able to maintain the required regulated output voltages up to a lateral displacement of 0.6 cm. Beyond this distance, the transferred power became insufficient to sustain the nominal output voltages, so the MP8859 input voltage was increased. In particular, the overall efficiency of the NerveRepack receiver decreased from 10.0% at 0.2 cm to 4.1% at 1.2 cm, while the Rewire receiver showed a reduction from 8.7% to 3.5% over the same displacement range.
The angular misalignment tests further highlighted the sensitivity of the system to coil positioning, since tilting the transmitter coil reduces the effective magnetic flux coupled to the receiver coil. The total efficiency of the NerveRepack receiver decreased from 10.0% at 2° to 5% at 14°, while the Rewire receiver showed a reduction from 8.28% to 4.3% over the same displacement range. As a result, both lateral and angular misalignments were identified as the most critical non-ideal operating conditions, as they can prevent the receiver from delivering the required regulated output voltages. These results emphasize the importance of accurate mechanical alignment between the external transmitter and the implanted receiver to ensure reliable and efficient wireless power transfer.

Chapter 7

Conclusion and Future Perspectives

The design of wireless power transfer (WPT) receivers operating at 13.56 MHz for implantable neuromodulation applications has been presented. Different WPT techniques were reviewed, highlighting Near-Field Resonant Inductive Coupling (NRIC) as the most suitable solution for Active Implantable Medical Devices (AIMDs) due to its ability to provide adequate power levels over transmission distances comparable to the thickness of biological tissues while maintaining high efficiency and safe operating frequencies.

The main design requirements considered for the implementation of WPT in AIMDs included: high power transfer efficiency, reduced receiver dimensions, and low sensitivity to coil misalignment. Based on these requirements, two receiver architectures were developed within the NerveRepack and Rewire projects. The resulting systems consist of four main functional blocks: the inductive link, the impedance matching network, the Class-E rectifier, and the DC/DC conversion stage.

Several design strategies aimed at maximizing the overall efficiency at low power transmission levels were investigated. Among them, the correct tuning of the matching network proved to be one of the most critical aspects in the receiver development. This is because the matching network directly affects the impedance seen by the receiving coil and, consequently, the amount of power that can be effectively transferred to the rectifier stage. At low transmitted power levels, even small mismatches can lead to a significant reduction of the voltage available at the rectifier input, preventing the DC/DC converters from operating in their input voltage range. Moreover, the matching network must be tuned to maximize the power delivered to the load and compensate variations of the coupling coefficient, the coil parameters, and the load condition, since the equivalent impedance of the inductive link depends on them. Furthermore, the Class-E rectifier demonstrated superior efficiency compared to alternative rectification approaches, making it particularly suitable for low-power implantable applications.

Simulation and experimental results showed that the overall efficiency increases as the load power increases. For the NerveRepack receiver, the overall efficiency increased from 10.5% at the minimum operating condition of 16 mW to 33.9% at 100 mW. Similarly, the Rewire receiver achieved efficiencies ranging from 8.9% at 24 mW to 19.4% at 100 mW.

The experimental results were compared with the LTspice simulations in order to evaluate the agreement between the predicted and measured behavior of the receiver. For both the receivers, the laboratory measurements showed lower overall efficiency than the simulations at all output power levels. This discrepancy can be attributed to several non-ideal effects that are difficult to fully model in simulation, including parasitic resistances, coil and PCB trace losses, component tolerances, imperfect tuning of the matching network, and additional losses introduced by the rectifier and DC/DC converter stages. Nevertheless, the measured efficiency followed the same increasing trend observed in simulation, confirming the validity of the design approach and showing that the receiver performance improves as the delivered output power increases. Additional measurements performed under vertical, lateral, and angular coil misalignment conditions confirmed the strong dependence of the system performance on the coupling coefficient between the transmitter and receiver coils.

Both receiver circuits were successfully implemented on printed circuit boards designed with future implantability in mind. The final dimensions were 56.7 mm $\times$ 21.8 mm for the NerveRepack receiver and 68.9 mm $\times$ 30.9 mm for the Rewire receiver. The final PCB size was mainly influenced by the discrete implementation of the power management stages, the use of commercially available inductors and trimmer capacitors in the matching network, and the need to maintain sufficient spacing between high-frequency traces and components to reduce parasitic effects. In addition, the receiver coil and the output connectors/test points used for experimental characterization contributed to increasing the overall board area. Although these dimensions are not yet fully compatible with long-term implantation, they demonstrate the feasibility of the proposed architectures and provide a solid basis for future miniaturization efforts.

Future work may focus on further reducing the PCB dimensions through higher levels of integration and the use of smaller passive components. Additional investigations should include thermal characterization and the implementation of a temperature monitoring system to prevent excessive heating of the surrounding tissues. Long-term reliability studies, electromagnetic safety analyses, and validation under realistic implantation conditions will also be necessary to move toward fully implantable wireless neuromodulation systems.

Bibliography

[1] Scott Stanslaski, Jeffrey Herron, Tom Chouinard, Duane Bourget, Ben Isaacson, Vaclav Kremen, Enrico Opri, William Drew, Benjamin H. Brinkmann, Aysegul Gunduz, Tom Adamski, Gregory A. Worrell, and Timothy Denison. A chronically implantable neural coprocessor for investigating the treatment of neurological disorders. *IEEE Transactions on Biomedical Circuits and Systems*, 12(6):1230–1245, 2018.

[2] Anubhav Bussooa, Steven Neale, and John R. Mercer. Future of smart cardiovascular implants. *Sensors*, 18(7), 2018.

[3] Annarita Cutrone and Silvestro Micera. Implantable neural interfaces and wearable tactile systems for bidirectional neuroprosthetics systems. *Advanced Healthcare Materials*, 8(24):1801345.

[4] W.J. Heetderks. Rf powering of millimeter- and submillimeter-sized neural prosthetic implants. *IEEE Transactions on Biomedical Engineering*, 35(5):323–327, 1988.

[5] Junho Kim, Hyeok Kim, Dongwook Kim, Hun-Jun Park, Kiwon Ban, Seungyoung Ahn, and Sung-Min Park. A wireless power transfer based implantable ecg monitoring device. *Energies*, 13(4), 2020.

[6] Fabian L. Cabrera and Fernando Rangel de Sousa. Achieving optimal efficiency in energy transfer to a cmos fully integrated wireless power receiver. *IEEE Transactions on Microwave Theory and Techniques*, 64(11):3703–3713, 2016.

[7] Intan Technologies. *RHS2116 Digital Stimulation and Recording chip.* Intan Technologies, LLC, Los Angeles, CA, USA. Datasheet.

[8] GBD 2021 Nervous System Disorders Collaborators. Global, regional, and national burden of disorders affecting the nervous system, 1990–2021: A systematic analysis for the global burden of disease study 2021. *The Lancet Neurology*, 23(4):344–381, 2024.

[9] European Parliament and Council. Regulation (EU) 2017/745 on medical devices. *Official Journal of the European Union*, 2017. L 117/1.

[10] Oscar Aquilina. A brief history of cardiac pacing. *Images in Paediatric Cardiology*, 8(2):17–81, 2006.

[11] Farooq Faisal, Muhammad Zada, Hyoungsuk Yoo, Ismail Ben Mabrouk, Mohamed Chaker, and Tarek Djerafi. An ultra-miniaturized antenna with ultra-wide bandwidth for future cardiac leadless pacemaker. *IEEE Transactions on Antennas and Propagation*, 70(7):5923–5928, 2022.

[12] Marcus Yip, Rui Jin, Hideko H. Nakajima, Konstantina M. Stankovic, and Anantha P. Chandrakasan. A fully-implantable cochlear implant SoC with piezoelectric middle-ear sensor and arbitrary waveform neural stimulation. *IEEE Journal of Solid-State Circuits*, 50(1):214–229, January 2015.

[13] Martin Jakobs, Manja Kloß, Andreas Unterberg, and Karl Kiening. Rechargeable internal pulse generators as initial neurostimulators for deep brain stimulation in patients with movement disorders. *Neuromodulation: Technology at the Neural Interface*, 21(6):604–610, 2018.

[14] Xiong Ying Liu, Ze Tao Wu, Yi Fan, and Emmanouil M Tentzeris. A miniaturized csrr loaded wide-beamwidth circularly polarized implantable antenna for subcutaneous real-time glucose monitoring. *IEEE Antennas and Wireless Propagation Letters*, 16:577–580, 2016.

[15] Syed Ahson Ali Shah and Hyoungsuk Yoo. Scalp-implantable antenna systems for intracranial pressure monitoring. *IEEE Transactions on Antennas and Propagation*, 66(4):2170–2173, 2018.

[16] Han Wang, Yuan Feng, Feng Hu, and Yong-Xin Guo. A wideband dual-polarized ring-loaded cross bowtie antenna for wireless capsule endoscopes: Design and link analysis. *IEEE Transactions on Antennas and Propagation*, 70(9):7843–7852, 2022.

[17] Sadeque Reza Khan, Sumanth Kumar Pavuluri, Gerard Cummins, and Marc P. Y. Desmulliez. Wireless power transfer techniques for implantable medical devices: A review. *Sensors*, 20(12):3487, 2020.

[18] imec. The medical implants of the future: Faster, smarter and more connected, April 2020. Published in imec Magazine, April 2020.

[19] Hyeonseok Kim, Bruno Rigo, Gabriella Wong, Yoon Jae Lee, and Woon-Hong Yeo. Advances in wireless, batteryless, implantable electronics for real-time, continuous physiological monitoring. *Nano-Micro Letters*, 16:52, 2024.

[20] Kadir A. Yildiz, Alexander Y. Shin, and Kenton R. Kaufman. Interfaces with the peripheral nervous system for the control of a neuroprosthetic limb: A review. *Journal of NeuroEngineering and Rehabilitation*, 17(43), 2020.

[21] Stanisa Raspopovic, Giacomo Valle, and Francesco Maria Petrini. Sensory feedback for limb prostheses in amputees. *Nature Materials*, 20:925–939, 2021.

[22] Sadeque Reza Khan, Sumanth Kumar Pavuluri, Gerard Cummins, and Marc P. Y. Desmulliez. Wireless power transfer techniques for implantable medical devices: A review. *Sensors*, 20(12):3487, 2020.

[23] NerveRepack Consortium. Nerverepack: Intelligent neural system for bidirectional connection with exoprostheses and exoskeletons. https://www.nerverepack.eu/, 2026. Accessed: 2026-05-15.

[24] Politecnico di Torino. Rewire - resonant wireless power transfer for implantable medical devices. https://elions.polito.it/home/biomedical-intelligent-systems/neuroprosthetics/rewire/, 2026.

[25] Jianming Zhao and Yuan Gao. A 13.56 MHz wireless power transfer system with bidirectional data link and closed-loop power control for implantable neuromuscular stimulator. In *2019 IEEE Asia-Pacific Microwave Conference (APMC)*, pages 1002–1004, New Delhi, India, 2019. IEEE.

[26] A. Essa et al. Wireless power transfer for implantable medical devices: A review. *Journal Name*, page 743, 2024.

[27] Han-Joon Kim, Hiroshi Hirayama, Sanghoek Kim, Ki Jin Han, Rui Zhang, and Ji-Woong Choi. Review of near-field wireless power and communication for biomedical applications. *IEEE Access*, 5:21264–21285, 2017.

[28] Pablo Pérez-Nicoli, Fortunato Dualibe, and Fernando Silveira. *Inductive Links for Wireless Power Transfer: Fundamental Concepts for Designing High-efficiency Wireless Power Transfer Links*. SpringerBriefs in Applied Sciences and Technology. Springer Nature, 2021.

[29] OSHA Cincinnati Laboratory. Electromagnetic radiation: Field memo, electromagnetic radiation and how it affects your instruments. Technical report, United States Department of Labor, Occupational Safety and Health Administration (OSHA), Cincinnati, OH, 1990.

[30] Naoki Shinohara. History of research and development of beam wireless power transfer. In *2018 IEEE Wireless Power Transfer Conference (WPTC)*, pages 1–3. IEEE, 2018.

[31] Tao Sun, Xiang Xie, and Zhihua Wang. *Wireless Power Transfer for Medical Microsystems*. SpringerBriefs in Electrical and Computer Engineering. Springer-Verlag, New York, NY, 2013.

[32] Masood Rehman et al. Wireless power transfer for implantable medical devices: Foundations, challenges, and future directions. *IEEE Access*, 11:144981–145015, 2023.

[33] Zhe Liu, Tong Li, Siqi Li, and Chunting Chris Mi. Advancements and challenges in wireless power transfer: A comprehensive review. *Nexus*, 1(2):100014, 2024.

[34] Jiejian Dai and Daniel C. Ludois. A survey of wireless power transfer and a critical comparison of inductive and capacitive coupling for small gap applications. *IEEE Transactions on Power Electronics*, 30(11):6017–6029, 2015.

[35] Hao Jiang, Junmin Zhang, Di Lan, K. K. Chao, Shysheng Liou, Hamid Shahnasser, Richard Fechter, Shinjiro Hirose, Michael R. Harrison, and Shuvo Roy. A low-frequency versatile wireless power transfer technology for biomedical imants. *IEEE Transactions on Biomedical Circuits and Systems*, 7(4):526–535, 2013.

[36] Kush Agarwal, Rangarajan Jegadeesan, Yong-Xin Guo, and Nitish V. Thakor. Wireless power transfer strategies for implantable bioelectronics. *IEEE Reviews in Biomedical Engineering*, 10:136–161, 2017.

[37] Masood Rehman, Sohrab Mirsaeidi, Nursyarizal Mohd Nor, Mohsin Ali Koondhar, Muhammad Ammirul Atiqi Mohd Zainuri, Zuhair Muhammed Alaas, Elsayed Tag-Eldin, Nivin A. Ghamry, and M. M. R. Ahmed. A review of inductive power transfer: Emphasis on performance parameters, compensation topologies and coil design aspects. *IEEE Access*, 11:144978–145010, 2023.

[38] Mohammad Haerinia and Reza Shadid. A state-of-the-art review on wireless power transfer approaches for implantable medical devices. *Energies*, 13(11):2837, 2020.

[39] Sols Miziev, Wiktoria Agata Pawlak, and Newton Howard. Comparative analysis of energy transfer mechanisms for neural implants. *Frontiers in Neuroscience*, 17, 2024.

[40] Saad Mutashar. Efficiency improvement of wireless power transmission for bio-implanted devices. *International Journal of Biomedical Engineering*, 7:721–724, 09 2013.

[41] H. Zou et al. Nfc/rfid-enabled wearables and implants for biomedical applications. *Microsystems & Nanoengineering*, 2025.

[42] Gian Luca Barbruni, Paolo Motto Ros, Danilo Demarchi, Sandro Carrara, and Diego Ghezzi. Miniaturised wireless power transfer systems for neurostimulation: A review. *IEEE Transactions on Biomedical Circuits and Systems*, 14(6):1160–1178, 2020.

[43] Damiano Merlin. Inductive power transfer class-e amplifier design for active implantable medical devices. Master's degree thesis, Politecnico di Torino, Turin, Italy, 2022.

[44] Sungryul Huh, Bumjin Park, Semin Choi, Yujun Shin, Haerim Kim, Jongwook Kim, Jaehyoung Park, Dongryul Park, and Seungyoung Ahn. Transmitter coils selection method for wireless power transfer system with multiple transmitter coils and single receiver coil. *IEEE Transactions on Power Electronics*, 38(3):4092–4109, 2023.

[45] Fabio Corti, Vittorio Bertolini, Antonio Faba, Ermanno Cardelli, and Alberto Reatti. Design procedures for series–series wpt systems: A comparative analysis. *Energies*, 17(5):1142, 2024.

[46] Amritansh Sagar, Manuele Bertoluzzo, and Abhay Kumar. Analysis and comprehensive comparison of wireless power transfer system using ss and sp topology for electric

vehicle charging. In *2023 International Conference on Computational Intelligence, Communication Technology and Networking (CICTN)*, pages 235–240, 2023.

[47] Krithikaa Mohanarangam, Yellappa Palagani, and Jun Rim Choi. Evaluation of Specific Absorption Rate in three-layered tissue model at 13.56 MHz and 40.68 MHz for inductively powered biomedical implants. *Sensors*, 23(2):749, 2023.

[48] CENELEC. Active implantable medical devices – part 1: General requirements for safety, marking and for information to be provided by the manufacturer. Standard EN 45502-1, European Committee for Electrotechnical Standardization, Brussels, Belgium, 2015.

[49] Fabiana Del Bono, Andrea Bontempi, Andrea Dentis, Nicola Di Trani, Danilo Demarchi, Alessandro Grattoni, and Paolo Motto Ros. Design of a closed-loop wireless power transfer system for an implantable drug delivery device. *IEEE Transactions on Biomedical Circuits and Systems*, 18(3):612–623, 2024.

[50] Mariusz Bojarski, Erdem Asa, and Dariusz Czarkowski. Effect of wireless power link load resistance on the efficiency of the energy transfer. In *2014 IEEE International Electric Vehicle Conference (IEVC)*, 2014.

[51] Mani Soma, Douglas C. Galbraith, and Robert L. White. Radio-frequency coils in implantable devices: Misalignment analysis and design procedure. *IEEE Transactions on Biomedical Engineering*, BME-34(4):276–282, 1987.

[52] Jason P. Wright, Ibrahim T. Mughrabi, Jason Wong, Jose Mathew, Naveen Jayaprakash, Christine Crosfield, Eric H. Chang, Sangeeta S. Chavan, Kevin J. Tracey, Valentin A. Pavlov, Yousef Al-Abed, Theodoros P. Zanos, Stavros Zanos, and Timir Datta-Chaudhuri. A fully implantable wireless bidirectional neuromodulation system for mice. *Frontiers in Neuroscience*, 18, 2024.

[53] Samuel Lienemann, Mary J Donahue, Johan Zötterman, Simon Farnebo, and Klas Tybrandt. A soft and stretchable multielectrode cuff for selective peripheral nerve stimulation. *Advanced Materials Technologies*, 8(6):2201322, 2023.

[54] Francisco Zurita, Leroy Grob, Amelie Erben, Fulvia Del Duca, Hauke Clausen-Schaumann, Stefanie Sudhop, Oliver Hayden, and Bernhard Wolfrum. Fully 3d-printed cuff electrode for small nerve interfacing. *Advanced Materials Technologies*, 8(3):2200989, 2023.

[55] Alejandro Carnicer-Lombarte, Alexander J Boys, Amparo Güemes, Johannes Gurke, Santiago Velasco-Bosom, Sam Hilton, Damiano G Barone, and George G Malliaras. Ultraconformable cuff implants for long-term bidirectional interfacing of peripheral nerves at sub-nerve resolutions. *Nature Communications*, 15(1):7523, 2024.

[56] Analog Devices. *LTC3129-1: 15V, 200mA Synchronous Buck-Boost DC/DC Converter with 1.3μA Quiescent Current.* Analog Devices, 2021. Datasheet.

[57] Analog Devices. *LTC660: 100mA CMOS Voltage Converter*. Analog Devices, 2003. Datasheet.

[58] D. Maksimovic and S. Dhar. Switched-capacitor dc-dc converters for low-power on-chip applications. In *30th Annual IEEE Power Electronics Specialists Conference. Record. (Cat. No.99CH36321)*, volume 1, pages 54–59 vol.1, 1999.

[59] Analog Devices. *LT3471: Dual 1.3A, 1.2MHz Boost/Inverter in 3mm × 3mm DFN*. Analog Devices, 2007. Datasheet.

[60] Tektronix, Inc. Introduction to VNA basics. Application Note 55W-60585-0, Tektronix Application Note, Beaverton, OR, USA, 2016.

[61] Matthew Schormans, Virgilio Valente, and Andreas Demosthenous. Practical inductive link design for biomedical wireless power transfer: A tutorial. *IEEE Transactions on Biomedical Circuits and Systems*, 12(5):1112–1130, 2018.

[62] Muh-Dey Wei and Renato Negra. Voltage-double RF rectifier using inductive matching network. In *Proceedings of the 2014 German Microwave Conference (GeMiC)*, pages 1–4. IEEE, 2014.

[63] Avishek Munsi, Sushan Pradhan, and Kunwar Aditya. Advancements in inductive wireless power transfer: A comprehensive review. *IEEE Transactions on Power Electronics*.

[64] Juan A. Santiago-González, Khurram K. Afridi, and David J. Perreault. Design of resistive-input class e resonant rectifiers for variable-power operation. *IEEE Transactions on Power Electronics*, 31(6):4356–4368, 2016.

[65] onsemi. *MMBD452LT1G: Dual Hot-Carrier Schottky Barrier Diodes*. onsemi, revision 6 edition, December 2024. Datasheet.

[66] Thomas H Lee. *Planar microwave engineering: a practical guide to theory, measurement, and circuits*, volume 1. Cambridge university press, 2004.

[67] X-Calculator. L matching network calculator, 2025. Accessed: 2026-01-12.

[68] Ali M. Niknejad. Matching networks, 2025. Integrated Circuits for Communication course slides.

[69] Coilcraft, Inc. *Chip Inductors – 1206CS Series (3216)*. Coilcraft, August 2022. Datasheet, accessed June 2026.

[70] Coilcraft, Inc. *Chip Inductors – 1812CS Series (4532)*. Coilcraft, August 2022. Datasheet, accessed June 2026.

[71] Coilcraft. *SPICE Model – 1206CS*. Coilcraft, Inc., March 2009. Revised 03/16/09. Accessed: 2026-05-26.

[72] Nurcan Keskin and Huaping Liu. Tuning of a wireless power transfer system with a hybrid capacitor array. *Wireless Power Transfer*, 2016.

[73] Andrea Dentis, Letizia Cantore, Stefano Concadoro, Danilo Demarchi, and Paolo Motto Ros. A 13.56 mhz inductive wireless power transfer system for active implantable medical devices. In *2025 32nd IEEE International Conference on Electronics, Circuits and Systems (ICECS)*, pages 1–4, 2025.

[74] C.K.H.C.K. Yahaya, Farid Adnan, Murizah Kassim, Ruhani Rahman, and Mohamad Rusdi. Analysis of wireless power transfer on the inductive coupling resonant. *Indonesian Journal of Electrical Engineering and Computer Science*, 12:592–599, 11 2018.